

417302

Sandia National Laboratories

Albuquerque, New Mexico 87185-1341

date: April 24, 1996

to: NWM Records Center, SWCF-A:WBS1.2.07.1:PDD:QA: Non-Salado:Culebra Transmissivity Zone:CLIMTIDX/GLOBAL



from: Thomas Corbet, MS-1324 (6115)

subject: Non-Salado Record Package: Culebra Transmissivity Zone: Climate Index

The attached record package contains the parameter value and supporting documentation for the Climate Index (idpram: CLIMTIDX, idmtrl: GLOBAL, id: 223). This record package is supported by several other record packages which will be submitted to the NWM Records Center at a later date (see also "Roadmap" contained in Part 2 of this package).

The information in this record package was collected by Principle Investigators for input to the WIPP Data Entry Form (Form 464) and for use by Performance Assessment personnel making parameter estimates. The record package was prepared in accordance with WIPP Quality Assurance Procedure (QAP) 17-1, WIPP QA Records Source Requirements.

Please call me at 848-0714 if you have any questions.

SWCF-A:WBS 1.2.07.1:PDD:QA:Non-Salado:Culebra Transmissivity
Zone:CLIMTIDX/GLOBAL

RECORDS PACKAGE:

NON-SALADO PARAMETERS REQUIRED FOR SECOFL2D:

CLIMATE INDEX

Purpose: The information contained in this package was collected by Principle Investigators as the basis for parameter estimates for input to the WIPP Data Entry Form and for use by Performance Assessment personnel.

Date of Record: 24 April, 1996

Authors/Organization: Thomas Corbet, Sandia National Laboratories, (505)848-0714, MS
1324

Peter Swift, Sandia National Laboratories, (505)848-0699, MS
1341

Recipient: NWM Records Center

File Code: SWCF-A:WBS 1.2.07.1:PDD:QA:Non-Salado:Culebra
Transmissivity Zone:CLIMTIDX/GLOBAL

TABLE OF CONTENTS

| Section | Contents | Page |
|---------------------------------|---|------|
| Part 1: Analysis Summary | | |
| A | Parameter Identification | 3 |
| B | Parameter Value | 3 |
| C | Scope and Objectives | 3 |
| D | Approach and assumptions | 4 |
| E | Modeling Results and Discussion | 14 |
| F | Rational for the Distribution for the Climate Index | 16 |
| G | References | 19 |
| H | Tables | 22 |
| I | Figures | 33 |

Total number of pages in Part 1 is 40.

Part 2: Analysis Documentation

| | | |
|---|--|----|
| A | Quality Assurance Status | 43 |
| B | Roadmap to Supporting Information for this Records Package | 43 |
| C | Identification of Individuals Who Performed the Work Reported in this Records Package | 43 |
| D | Training and Certification Requirements | 43 |
| E | Identification of Computer Software and Hardware | 44 |
| F | Identification of Inputs and Sources | 44 |
| G | Documentation of Review of Work | 45 |

Total number of pages in Part 2 is 6.

| | | |
|-------------|------------------------------------|----|
| Appendix 1. | User's Manual for SECOFL3D Version | 49 |
|-------------|------------------------------------|----|

Total number of pages in Appendix 1 is 43.

PART 1: ANALYSIS SUMMARY

A. Parameter Identification

| | |
|------------------------|---------------|
| parameter description: | Climate Index |
| idpram: | CLIMTIDX |
| idmtrl: | GLOBAL |
| id#: | 223 |

B. Parameter Value

The constructed distribution (subjective) is as follows: the probability density is 3.0 in the interval from 1.0 to 1.25 and the probability density is 0.333 in the interval from 1.5 to 2.25. Consequently, the probability that a sampled value of the Climate Index is in the interval from 1.0 to 1.25 is 0.75, and the probability that a value is in the interval from 1.5 to 1.25 is 0.25.

C. Scope and Objectives

Scenarios involving one or more intrusion holes consider the possibility that brine carrying radionuclides in solution could flow up an intrusion hole and then flow laterally in the Culebra Dolomite Member to the accessible environment. A change in climate could alter the flow rates and directions of groundwater flow in the Culebra and consequently impact transport of radionuclides to the accessible environment. The performance assessment calculations for the CCA will include the possible effect of climate change on transport in the Culebra by multiplying the magnitude of flow in each realization of the Culebra flow field by a sampled value of the Climate Index. This will uniformly modify flow rates, but not flow directions, in each realization of the Culebra flow-field.

The objective of this analysis is to specify the sample distribution for the Climate Index. This is a constructed subjective distribution because it is not possible to directly measure future changes in climate or their long-term effect on groundwater flow in the Culebra. The rationale for the distribution has two main parts. First we have surveyed the scientific literature to find available information that can be used to infer the annual precipitation rate since the end of the Pleistocene and for the next 10,000 years. Second, we performed a series of numerical simulations to see how various assumed rates and temporal patterns of recharge would impact groundwater flow velocities in the Culebra within the WIPP site.

This parameter records package is in two parts. The remainder of this Part 1 outlines the approach and assumptions used in this analysis (Section D), the results of the numerical simulations (Section E) and finally, in Section F, the rationale for the specified distribution for the Climate Index. Part 2 contains details of the analysis documentation.

D. Approach and Assumptions

Climate Change

Geologic data from southeastern New Mexico and the surrounding region show repeated alternations of wetter and drier climates throughout the Pleistocene, corresponding to global cycles of glaciation and deglaciation. Data from plant and animal remains and paleo-lake levels permit quantitative climate reconstructions for the region only for the last glacial cycle, and confirm the interpretation that conditions were coolest and wettest during glacial maxima (Swift, 1993). The hottest and driest conditions since the last glaciation have been similar to those of the present. Modeling of global circulation patterns suggests that these changes resulted from the disruption and southward displacement of the winter jet stream by the ice sheet, causing an increase in the frequency and intensity of winter storms throughout the American Southwest (COHMAP Members, 1988). Mean annual precipitation 22,000 to 18,000 years ago, when the last North American ice sheet reached its southern limit roughly 1500 km north of the WIPP, was approximately twice that of the present (Figure 1). Mean annual temperatures may have been as much as 5°C colder than at present.

Glacial periodicities have been stable for the last 800,000 years (Milankovitch, 1941; Hays et al., 1976; Imbrie et al., 1984; Imbrie, 1985). Barring anthropogenic changes in the Earth's climate, relatively simple modeling of climatic response to orbital changes in insolation suggests that the next glacial maximum will occur in approximately 60,000 years (Imbrie and Imbrie, 1980). The extent to which unprecedented anthropogenic climate changes may alter this conclusion is uncertain, but presently available models of climatic response to an enhanced greenhouse effect (e.g., Mitchell, 1989; Houghton et al., 1990) do not predict changes of a larger magnitude than those of the Pleistocene. Furthermore, published models do not suggest significant increases in precipitation in southeastern New Mexico following global warming (Washington and Meehl, 1984; Wilson and Mitchell, 1987; Schlesinger and Mitchell, 1987; Houghton et al., 1990).

Relatively shorter-term climatic fluctuations in southeastern New Mexico have occurred throughout the Pleistocene and Holocene with periodicities on the scale of thousands of years (Figure 1). The causes of these nonglacial fluctuations are, in general, unknown, but paleoclimatic data indicate that precipitation may have approached glacial highs for relatively short periods at some times during the Holocene (Swift, 1993). Based on the past record, fluctuations of this sort are possible and perhaps likely during the next 10,000 years.

Numerical Modeling of Groundwater Flow

The overall approach of the numerical modeling was to perform a series of simulations of groundwater flow in the strata overlying the Salado Formation assuming a range of values for the hydraulic properties of the rocks, recharge rates, and changes in recharge rate with time. We examine the simulation results to see how the lateral flow out of the portion of the Culebra within

the WIPP site change over the next 10,000 years. The uncertainty in the hydraulic properties of units other than the Culebra is large and the number of simulations that can be performed is limited. We therefore subjectively select combinations of hydraulic parameters that represent a broad range of possible responses to future changes in recharge.

CONCEPTUAL MODEL

These numerical simulations are based on the widely-accepted concepts of regional groundwater flow in groundwater basins (Hubbert, 1940; Tóth, 1963; Freeze and Witherspoon, 1967). A groundwater basin is a three-dimensional closed hydrologic unit bounded on the bottom by an "impermeable" rock unit (actually a stratigraphic layer with much smaller permeability than the layers above), on the top by the ground surface and on the sides by groundwater divides. The upper boundary of the region of saturated flow is the water table. All rocks in the basin have finite permeability, i.e., hydraulic continuity exists throughout the basin. All recharge to the basin is by percolation of precipitation to the water table and all discharge from the basin is by flow across the water table to the land surface. Here, the term recharge is used as defined by Freeze and Cherry (1979) to mean the entry into the saturated zone of water made available at the water-table surface, together with the associated flow away from the water table within the saturated zone.

Differences in the elevation of the water table across the basin provide the driving force for groundwater flow. The pattern of groundwater flow depends on the lateral extent of the basin, the shape of the water table, and the heterogeneity of the permeability of the rocks in the basin. Water flows along gradients of hydraulic head from regions of high head to regions of low head. The highest and lowest heads in the basin occur at the water table at its highest and lowest points respectively. Therefore groundwater generally flows from the elevated regions of the water table, downward across confining layers (layers with relatively low permeability), then laterally along more conductive layers, and finally upward to exit the basin in regions where the water table (and by association, the land surface) is at low elevations.

The position of the water table moves up and down in response to changes in recharge. The water table can't rise higher than the land surface at any location. Seepage faces develop in areas where recharge is sufficient to maintain the water table at the land surface. It is through the development of seepage faces that the topography of the land surface impacts patterns of groundwater flow. Seepage faces occur only in topographically low areas if recharge is low. In this case, groundwater flow is toward the seepage faces. The portion of a basin that is covered by seepage faces increases as recharge increases. Given a sufficiently humid climate, the entire surface of a groundwater basin is covered by seepage faces. That is, the water table is everywhere close to the land surface. As groundwater flow adjusts to changes in recharge, the rise or fall of the water table is greatest under areas in which the elevation of the land surface is highest.

Climate impacts groundwater flow by changing the amount of moisture that infiltrates and recharges the saturated zone. In our implementation of this conceptual model, changes in

climate are represented as changes in the rate of potential recharge with time. We assume that more recharge occurs during cool wet climates than during hot dry climates.

TOPOGRAPHY AND MODEL BOUNDARIES

The lateral boundary of the numerical model for the WIPP region (Figure 2) coincides with selected topographic depressions and highs on the land surface. The boundary follows Nash Draw and the Pecos River valley to the west and south and the San Simon Swale to the east. The boundary continues up drainages and dissects topographic highs along the northern part of its east side. It is assumed that these boundaries represent groundwater divides whose position remains fixed over the range of past and future climates. There are other groundwater divides within this boundary. The positions of these additional divides might change with time and, in some cases, even their existence might be intermittent. The lower boundary of the model is the top of the Salado Formation and the upper boundary coincides with the land surface.

HYDROSTRATIGRAPHY

Measurements of rock hydraulic properties are available for only a tiny fraction of model area because this area is much larger (it covers approximately 6000 square kilometers) than the region covered by the site characterization. Values for these properties are inferred from geologic observations and conceptual models of how geologic processes have altered hydraulic properties.

The strata above the Salado are layered and there are large differences in the ease at which water can flow through the individual layers. We conceptualize the effect of the layering on groundwater flow in terms of the hydrostratigraphic units (Figure 3) defined by Powers and Holt (1990). A hydrostratigraphic unit comprises one or more adjacent rock layers with similar hydrologic characteristics. The Powers and Holt classification divides the Rustler Formation and overlying strata into 13 hydrostratigraphic units. Those hydrostratigraphic units that are relatively more permeable are referred to here as conductive units and those with very small permeability are called confining layers. The confining layers consist of anhydrite and halite. Dolomite layers form the conductive units. The confining layers are perhaps five orders of magnitude less conductive than the dolomite units. Dividing the Rustler and overlying strata into 10 stratigraphic units is sufficient to represent vertical heterogeneity at the regional scale. A detailed examination, however, would show that each of these units is also vertically heterogeneous. Heterogeneity within a hydrostratigraphic unit effects, for example, the transport of radionuclides along that unit.

The hydrostratigraphic units account for vertical differences in hydraulic properties. Such differences are due to the sedimentary processes that were active as these rocks were deposited. However, the hydrologic properties of these rocks also vary laterally. It is thought that post-depositional geologic processes caused the lateral variations. Those processes that were accounted for in our assignment of hydraulic conductivity values are summarized below.

Salado Dissolution. The top of the Salado Formation has been dissolved over large

SWCF-A:WBS 1.2.07.1:PDD:QA:Non-Salado:Culebra Transmissivity Zone:CLIMTIDX/GLOBAL6

Information Only

areas. This dissolution disrupts and fractures Rustler strata and consequently increases their hydraulic conductivity to varying degrees. In the most extreme case, the Rustler breaks into blocks which rotate and are collapsed downward. In these regions, stratigraphic continuity is disrupted and vertical hydraulic conductivity increases to the extent that the Rustler does not behave hydrologically as a layered system. In other regions in which Salado dissolution is less extensive, stratigraphic continuity is maintained but fracturing increases the hydraulic conductivity of the more brittle carbonate and anhydrite units.

Dissolution of Pore- and Fracture-Filling Minerals. Evaporite minerals (halite, gypsum, or anhydrite) fill much of the pore space and fractures in intact Rustler units. Over portions of the map area, moving groundwaters have dissolved these minerals and have thereby locally increased hydraulic conductivity. For example, dissolution of cements and fracture fillings is thought to be an important control on the pattern of hydraulic conductivity of the Culebra dolomite in the vicinity of WIPP.

Proximity to Halite Deposits. In regions where halite deposits are present in the Rustler, halite replaces gypsum in the rock matrix and fills fractures in units that underlie or overlie the halite deposits. The hydraulic conductivity in units affected by gypsum replacement and fracture filling is possibly as low as that of the halite deposits.

The regions affected by the various geologic processes have been mapped into a series of zones. Figure 4 is a map of the extent of these zones. These zones, along with specification of hydrostratigraphic units, are used to infer the distribution of hydraulic conductivity values in numerical simulations. We use a two-step approach assign hydraulic conductivity values to cells within the numerical model. First an "intact" conductivity value is assigned to each rock type. This value represents the hydraulic conductivity of that rock type before the effect of post-depositional processes. The intact values assigned changed from simulation to simulation; the values used are given in Tables 1 and 2. Second, intact values are adjusted to reflect the impact of the post-depositional process in the zones shown in Figure 4. The amount of adjustment is based on measured values of hydraulic conductivity in each of these zones in the Culebra in the vicinity of the WIPP site. The following adjustments, in units of the logarithm of conductivity (m/s), are applied:

- upper Salado dissolution (zone 2), applied to dolomites and anhydrites: +1.0
- dissolution of fracture fillings (zones 2 and 3), applied to dolomites: +1.5
- presence of halite in adjacent layers (zone 5), applied to the Culebra: -2.0

RECHARGE RATES AND PATTERNS

In dry environments, such as the WIPP site, the fundamental effect of climate change on groundwater flow is to influence the position of the water table. The position of the water table, along with the distribution of the rock's hydraulic conductivity, determine flow directions and rates at depth. For this discussion, the process by which climate moves the water table can be divided into three parts, infiltration, percolation in the unsaturated zone, and recharge to the saturated zone. As discussed below, our model, and therefore the link between climate and groundwater flow, focuses on the last part, recharge to the saturated zone.

Evapotranspiration potential greatly exceeds annual precipitation in southeastern New Mexico and only a small portion of precipitation infiltrates below the root zone. The relationship between the rate and spatial distribution of infiltration and climatic factors is complex. Infiltration depends, for example, on the temporal and spatial pattern of precipitation, soil and plant types, land surface slopes, surface drainage, wind speeds, and air temperature and humidity. We clearly do not know these details about the future environment, nor do we need this information to estimate possible effects of climate on groundwater flow. Our model therefore does not consider the details of the interaction between climatic factors and infiltration.

After infiltration, moisture is available to infiltrate downward toward the water table. The pattern of flow is complex because the unsaturated hydraulic properties of the rocks are highly heterogeneous and variable in time. Where the water table is at depth the net movement of water is downward, but the lateral components of flow are such that the spatial pattern of percolation at the water table is different than the pattern at the land surface. It is not possible or necessary to characterize the unsaturated hydraulic properties at the scale of our model, nor do we need this information to estimate possible effects of climate on groundwater flow. Our model does not simulate flow in the unsaturated zone.

In these calculations, changes in climate are represented by changes in potential recharge at the water table. Potential recharge is the maximum amount of moisture available to recharge the saturated zone. Actual recharge is equal to potential recharge in areas where the water table is at depth, but can be less than potential recharge if the water table is near the land surface and a seepage face forms. The spatial and temporal distribution of potential recharge is specified as model input, but the distribution of recharge is a simulation result. We assume that potential recharge varies in time but is spatially uniform over the model domain because of the large uncertainty in its spatial distribution and the relative insensitivity of model results to spatially-varying recharge. The rate of potential recharge used in these simulations should be thought of as the water available to recharge the water table as averaged over the area of a model cell (4 square kilometers) and long periods of time (hundreds of years). This conceptual averaging is consistent with the resolution in modeling natural systems at this scale.

We vary potential recharge so that the hydraulic conditions range from conditions that are similar to those of today (water table at depth) to the limiting conditions that could occur in times of greater recharge (water table near the land surface). The values used for potential recharge are model specific in that they were selected to simulate a range of possible hydrologic conditions.

The validity of the results does not rest on demonstrating that these values are the same as past or future actual values. However, the values used are certainly reasonable. The rates used in these calculations ranged from 0.2 to 2.0 mm/year. The same range was determined by Campbell et al. (1996) using a chloride mass balance method to estimate localized infiltration rates at the WIPP site. They noted that these estimates are in agreement with studies in other similar geologic environments. In addition, we believe that these calculations provide the best possible estimates of the upper limit of recharge over large areas and long periods of time.

Both steady-state and transient calculations were used to evaluate the effects of climate on groundwater flow. Effects are implied from steady-state calculations by comparing results of calculations that differ only in the specified rate of potential recharge. These comparisons represent the maximum effect on flow that a change in recharge from one of the values to the other could have because the time lag in the response is not accounted for. Transient simulations, in contrast, show how the hydrologic system responds as the potential recharge changes with time.

We make two assumptions about past recharge conditions 1) that times of maximum precipitation are also times of maximum recharge and 2) recharge in the late Pleistocene was sufficient to raise the water table to near the land surface. Therefore, recharge sufficient to raise the water table to the land surface was assumed at the start of the transient simulations (i.e., at 14,000 years before present). We refer to this recharge rate as the late Pleistocene recharge rate. The potential recharge was assumed to decrease to zero (the Holocene minimum recharge rate) over 6,000 years. This portion of the recharge function represents the first-order feature of the precipitation record: that the average annual precipitation decreased starting about 14,000 years ago and reached a minimum about 8,000 years ago (Swift, 1993).

The remainder of the recharge function (Figure 5), covering the period from 8,000 years ago until 10,000 years in the future, represents the historical short-term wet periods as well as uncertainty about future precipitation rates and temporal patterns. The historical wet periods are represented by spikes in the recharge function that reach maximum recharge rates (maximum Holocene recharge rates) at 6,000, 4,000, and 2,000 years ago. Each spike has a duration of 1,000 years. We use different rates for the maximum Holocene recharge rate to represent uncertainty in that value but, within a single simulation, assume the same maximum rate for each wet period.

Because of uncertainty about the magnitude and duration of future climatic change, we use two patterns for future recharge. Either pattern is possible, given the present state of knowledge about future climates, but neither is presented here as a prediction of the future state. Rather, the two patterns, and the parameterization of potential recharge within each pattern, provide a distribution that reasonably represents our uncertainty about the effects of possible future climatic change on recharge. Both recharge patterns assume that recharge will be greater at some time in the future than it is at present, and that present recharge is the same as its minimum Holocene value (zero for this analysis, as discussed below). Both recharge patterns also

assume that the dominant effects on climate change during the next 10,000 years will be natural, rather than anthropogenic. In part, this assumption that natural effects will dominate is based on the observation noted in Section D that published model results suggest that if anthropogenic global warming occurs it will not result in an increase in precipitation in southeastern New Mexico. Furthermore, regulatory guidance provided by the EPA indicates that consideration of climatic change should be limited to natural processes (US EPA, 1996, p. 5277).

The first recharge pattern considered in the analysis assumes that recharge will increase from its minimum value at the present to its maximum Holocene value 500 years in the future. Recharge is then held constant after this "step" increase, and this pattern is therefore referred to as the "step pattern" of future recharge. As discussed below, the maximum Holocene value is varied between simulations to characterize uncertainty about the magnitude of the maximum value. Conceptually, the step pattern corresponds to a future in which the climatic patterns of the Holocene are disrupted, and the climate either becomes continuously wetter or the frequency of alternations between wetter and drier climates becomes sufficiently high that the hydrologic response is indistinguishable from that of a continuously wetter climate. Mechanisms that might produce this precipitation pattern and their probability of occurrence are discussed in Section F below.

The second recharge pattern used in this analysis is simply a continuation of the observed pattern of the Holocene, with an oscillatory recharge function with peaks occurring 500, 2,000, 4,000, 6,000, 8,000, and 10,000 years in the future. We refer to this pattern as the Holocene pattern of future recharge. Conceptually, this pattern corresponds to a continuation of the variability of the Holocene, with alternations of wetter and drier climates, and without major, first-order disruptions to the climatic cycles. The probability of occurrence of this pattern is discussed below in Section F.

The values used for the late Pleistocene, Holocene minimum, and Holocene maximum recharge rates for the transient simulations are shown in Table 3. We assume as an initial condition at 14,000 years ago a flow field that had equilibrated to a late Pleistocene recharge rate of 2.0 mm/yr for all the transient simulations. This is a somewhat arbitrary rate that was selected to be large enough to maintain the water table near the land surface for all of the distributions of hydraulic conductivity considered.

Values used for the maximum Holocene rates of potential recharge are 0.2, 0.4, or 0.6 mm/yr. This range is limited to those values that are not so large that they result in unrealistically high simulated heads for the present time. The largest value also results in future conditions similar to those assumed for the late Pleistocene if the step recharge function is used.

The choice to use a value of zero mm/yr for the minimum Holocene recharge rate is also somewhat arbitrary, and is not intended to imply that the actual present recharge rate is zero. For modeling purposes, the only requirement imposed on the minimum Holocene recharge rate is that it is a non-negative number that is sufficiently less than the lowest maximum Holocene value used

(0.2 mm/yr) to result in different flow conditions during the wet and dry Holocene periods. Flow in the transient simulations never approach equilibration with the minimum Holocene recharge rate. The main effect of choosing a value of zero for this rate is to maximize the steepness of the sloped portions of the recharge function, and consequently, to maximize the simulated impact of climate change.

MATHEMATICAL AND NUMERICAL MODEL

The groundwater-flow equations are solved on the saturated domain Ω , which is assumed to be an irregularly-shaped “box” with unknown moving top surface given by the water-table elevation Z_{WT} . The interior equation for the domain Ω is

$$\nabla \cdot \kappa \nabla h = S_s \frac{\partial h}{\partial t} \quad (1)$$

with κ a spatially-dependent conductivity tensor, S_s the specific storage coefficient.

Zero-gradient boundary conditions are assumed on the sides and bottom of the domain. On the top portion of Ω free-surface (or phreatic) boundary conditions are imposed (Bear and Verruijt, 1987; Dagan, 1989; de Marsily, 1986). Because the location of the water-table is not known *a priori*, two boundary conditions must be imposed at the water-table:

$$h(x, y, z_{WT}, t) = z_{WT}(x, y, t), \quad (2)$$

$$(\kappa \cdot \nabla h + N) \cdot \nabla (h - z) = \omega \frac{\partial h}{\partial t}, \quad (3)$$

with $N = -R \nabla z$ being the vertical infiltration rate. The first boundary condition is a statement that the pressure at the water-table surface is atmospheric. The second condition is the kinematic boundary condition (Bear and Verruijt, 1987) that assures that the flux normal to the surface is continuous.

If the recharge flux N is independent of time, an equilibrium or “steady-state” water-table develops. This condition physically represents the case of mass balance between fluid injected into the saturated zone by steady recharge and fluid lost due to the presence of seepage faces. For steady-state the SECOFL3D code uses the interior equation

$$\nabla \cdot \kappa \nabla h = 0. \quad (4)$$

The equilibrium water-table position is embodied in the condition $\partial h / \partial t = 0$, which reduces the

kinematic boundary condition to

$$(\nabla \cdot \kappa \nabla h + N) \cdot \nabla (h - z) = 0. \quad (5)$$

This equation shows that, to first-order, the equilibrium position reached in steady-state is due to a balance between surface recharge and vertical flow.

An additional complication in modeling free-surface groundwater flow is the need to simulate seepage flow wherein the water-table interacts with the land surface. The appropriate "seepage" boundary condition is (Bear and Verruijt, 1987; de Marsily, 1986):

$$h(x, y, z_{WT}, t) = z_{LS}(x, y), \quad (6)$$

which replaces the condition (2). The kinematic condition (3) is not enforced at seepage faces.

The kinematic condition is applied wherever the water-table elevation is below the land surface. If the water-table elevation is the same as the land surface, the kinematic condition may need to be converted to a seepage face. To determine whether the kinematic or the seepage boundary condition should be applied when the elevation of the water-table and the land surface are the same, we compute

$$U = R - (K_{33} + R) \partial h / \partial z + \nabla h \cdot \kappa \nabla h \quad (7)$$

Since $U = \omega \partial h / \partial t$, its algebraic sign indicates whether the water-table is rising or falling at a particular location. If the water-table is at the land surface and $U < 0$ it is assumed that the water-table is freely falling and thus the kinematic condition is called for. If $U \geq 0$ at the land surface, then the water-table is rising and the seepage condition is enforced as a Dirichlet boundary condition in the linearized system.

To solve these equations, the code SECOFL3D transforms the saturated domain onto a moving mesh to accommodate the changes in the domain with time. The transformed equations are then discretized using centered differences on a finite volume, staggered mesh. Because the free-surface flow equations are non-linear, the set of discrete equations must be linearized. This is done by means of a Picard Iteration. Additional details concerning the numerical model are provided by Knupp (1996).

The lateral extent of the model cells is 2 km on a side. This discretization of hydraulic properties is appropriate for the scale of this model but is much less detailed than the discretization used for distribution of Culebra transmissivity in performance assessment calculations. For this reason, these simulations provide a fundamentally different level of resolution of the flow field than do the performance assessment calculations.

PERFORMANCE MEASURE

The Climate Index increases flow magnitudes by the same factor at all locations within the flow fields used in the PA calculations. The index is applied uniformly because these simulations do not have the resolution to calculate its dependence on position. In order to conserve mass, this condition requires that the total flow across the boundary of an arbitrary closed portion of the flow field change by the same factor. We use this relationship to choose the total lateral flow out (essentially equal to total flow out) of a portion of the Culebra that is approximately within the WIPP-site boundary as the performance measure to base the Climate Index on. This portion of the Culebra is referred to as the Culebra reference volume. The surface trace of the reference volume is a square that is about the same area as the WIPP site but is shifted slightly to the northwest relative to the position of the WIPP site. The UTM coordinates of the corners of the WIPP site are N3585057, E610496; N3585109, E616941; N3578681, E617015; and N3578612, E610566. The UTM coordinates of the surface trace of the reference volume are N3586000, E610000E; N3586000, E616000; N3580000, E616000; and N358000, E610000.

In analyzing simulation results, we are concerned with how future rates of total lateral flow out of the Culebra reference volume compare to the simulated present rate. We refer to this as the lateral-flow ratio. For transient simulations, this is the ratio of the total lateral flow out of the Culebra reference volume at a given time in the future to that quantity at the simulated present time. For example, Table 7 shows that for transient simulation 30, the rate of lateral flow out of the Culebra reference volume is 3335 m³/yr at 10,000 years in the future. Table 6 shows that the value for this number is 2107 m³/yr at the simulated present time. The ratio of these numbers, as indicated in Table 8, is 1.6. This same value would be achieved by uniformly increasing the magnitude of lateral flow within the WIPP site by a factor of 1.6. Steady-state simulations, by definition, do not provide the rate of lateral flow at different times. The lateral-flow ratios for steady-state simulations (Table 5) are the ratios of total lateral flow out of the Culebra for pairs of calculations that differ only in their recharge rate.

SUMMARY OF ASSUMPTIONS

The main assumptions of the modeling approach are:

the groundwater basin conceptual model is applicable,

the lateral boundaries are flow divides (i.e. no-flow boundaries) during the period simulated,

flow in the unsaturated zone can be neglected, and

the flow system was equilibrated to a recharge rate sufficient to maintain the water table near the land surface at the start of the simulations.

E. Modeling Results and Discussion

We performed 54 steady-state and 17 transient simulations (Tables 1 - 3). Results are presented in two formats:

- 1) As mass balances over the Culebra reference volume.
- 2) Head values for each hydrostratigraphic unit at the WIPP site are graphed versus time for six of the transient simulations.

Steady-State Results

Table 4 shows the mass balances over the Culebra reference volume for the steady-state simulations. This table shows the rate of total flow across the surface of the reference volume as well as the percent of the total that flows in or out across the top, base, and sides. For example, the amount of simulated vertical leakage across the top of the Culebra reference volume ranges from 1.4 to 97.8 percent of the total inflow. More than 97.4 percent of the outflow from the Culebra reference volume is by lateral flow in all but one of the steady-state simulations.

Table 5 shows the lateral-flow ratios for the 27 pairs of steady-state simulations that differ only in the value of potential recharge. Each of these pairs includes a simulation with potential recharge equal to 2.0 mm/yr and a calculation with potential recharge equal to 0.2 mm/yr. The higher rate was sufficient to raise the water table at the center of the WIPP site to the land surface in all cases. In addition, the lower rate was sufficient to raise the water table to the surface in simulations 3, 12, and 21. The lateral-flow ratios for the pairs of steady-state simulations range from 0.7 to 5.5.

We use the vertical differences in head near the center of the WIPP site as an indicator of whether or not a particular set of hydraulic properties could be representative of actual conditions. Figure 6 shows the simulated elevation of the water table and values of hydraulic head in the Magenta and Culebra near the center of the WIPP site for the 27 simulations that assume a recharge rate of 0.2 m/yr. (We use the simulations with the lower recharge rate because these results best approximate actual present-day conditions.) Each graph in this figure presents head profiles from three simulations as a function of anhydrite conductivity. For each value of anhydrite conductivity in each graph, the three data points are the water table (upper point), Magenta head, and Culebra head (lower point). In each of the steady-state calculations, the difference in head between these units decreases as the conductivity of the anhydrite layers increases. Also, the difference in head between units is less than 10 m for all simulations that assume a value of 2×10^{-6} m/s for the conductivity of the Dewey Lake/Triassic rocks.

The simulated differences in head can be compared to observed differences. The actual

difference in fresh-water head between the Culebra and the Magenta is about 40 m. The difference between the head in the Magenta and the estimated position of the water table is 20 m. Using these numbers as guides, those simulations in which hydraulic conductivity of intact anhydrite is 1×10^{-11} m/s or the conductivity of the Dewey Lake/Triassic rocks is 2×10^{-6} stand out as resulting in unrealistically small differences in head. We have therefore excluded the lateral-flow ratios from these calculations (simulation pairs 1/28, 4/31, 7/34, 8/35, 9/36, 10/37, 13/40, 16/43, 17/44, 18/45, 19/46, 22/49, 25/52, 26/53, and 27/54) from consideration in determining the distribution of the Climate Index.

Transient Results

Vertical profiles of hydraulic head versus time provide an intuitive illustration of the effects of the recharge function on groundwater flow. A series of such graphs are presented in Figures 7, 8, and 9. These simulations use the same hydraulic properties (the properties for transient simulation number 30) and differ only in the pattern of future recharge and the maximum rate of Holocene recharge. In these figures, the upper-most line is the water table and the lower-most line represents head in the Culebra. The seven lines in between show head in the seven hydrostratigraphic units between the Culebra and the Dewey Lake. The order of the head lines is the same as their stratigraphic order.

Figure 7 (top), for example, shows the simulated hydraulic head with time if the maximum Holocene recharge is 0.2 mm/yr and the step pattern is used for future recharge. This graph illustrates several important aspects of the long-term behavior of the hydrologic system. First, the water table remains level for about 4,200 years after the start of the simulation. The water table does not drop even though the rate of potential recharge decreased over this time because over most of the range in change of recharge, the recharge is more than sufficient to maintain the water table at the land surface at WIPP. However, head in the Culebra decreased from the start of the simulation. This shows that flow in the Culebra responds to changes in the regional-scale flow system caused by the water table dropping faster in other parts of the model domain. Once, the water table becomes a free-surface at WIPP, heads in all layers begin to decrease more rapidly.

The overall trend over the first 14,000 years of the simulation was a decrease in the elevation of the water table and the heads in all strata. The water table dropped about 80 m and head in the Culebra dropped about 35 m. This overall trend reflects the decline in the rate of potential recharge from 2.0 to 0.0 mm/yr over the first 6,000 years of the simulation. Superimposed on the trend are short-term increases in heads that correspond to the periodic increases in potential recharge. The times of maximum head lag about 300 years behind the corresponding peaks on the recharge function.

Heads, in this simulation, increase continuously after the simulated present time. This increase represents the flow systems attempt to equilibrate with a recharge rate of 0.2 mm/yr that was assumed to occur for the simulated time period between 500 and 10,000 years in the future. Heads are still increasing at the end of the simulation. Given sufficient time, these heads would

reach the equilibrium elevations of steady-state calculation number 14.

Tables 6 and 7 show the mass balance for the Culebra reference volume at the present time and at 10,000 years in the future respectively. Table 8 shows the lateral-flow ratios at 10,000 years for each of the 17 transient simulations. These numbers range from 0.8 to 2.1. As can be inferred from the graphs of head versus time, the lateral-flow ratio reaches a maximum value at 10,000 years if the step pattern is used for future recharge. This is not the case if the Holocene pattern is used. We have therefore calculated the lateral-flow ratio as a function of time for the six transient simulations that use the Holocene pattern and graphed those results in Figure 10.

Figure 10 (top) shows the lateral-flow ratio for two sets of simulations (41, 42, and 43) that differ only in the value used for maximum Holocene recharge. This time-trace clearly shows the effects of the Holocene wet periods superimposed on the long-term decline of the lateral-flow ratio. The high frequency signature of the wet periods dominate the trend if the maximum Holocene recharge is 0.4 or 0.6 mm/yr. The long-term trend is more important if the recharge rate is 0.2 mm/yr. The lateral-flow ratio is less than 1 over nearly the entire 10,000-year future period at this lower maximum Holocene recharge rate. The trend in the lateral-flow ratio is similar for simulations 44, 45, and 46 (bottom).

F. Rationale for the Distribution for the Climate Index

Future Precipitation

Mechanisms that might produce a climate change corresponding to the step pattern of recharge are speculative. Based on the past climatic record, initiation of a new cycle of global cooling leading eventually to glaciation is possible within the next 10,000 years, and could perhaps disrupt the Holocene climatic patterns of southeastern New Mexico. However, a return to the full-glacial conditions of the late Pleistocene, in which the climate of southeastern New Mexico was affected by a continental ice sheet extending southward into the Great Plains, is not plausible within the next 10,000 years. Temperatures at high latitudes may have fluctuated abruptly during the late stages of the last major interglacial period approximately 120,000 to 110,000 years ago, but it is likely that climatic effects were less at lower latitudes (Dansgaard et al., 1993). Evidence from oxygen isotope ratios in ice cores and gases trapped within them indicates that changes in the total volume of continental ice sheets at the end of the last interglacial period do not correlate with changes in polar temperatures (Raynaud et al., 1993). Consideration of the oxygen isotope record from oceanic sediments suggests that major growth in continental ice sheets did not occur until late in the last glacial period, many tens of thousands of years after the end of the last interglacial (Imbrie et al., 1984). Relatively little is known about precipitation patterns in southeastern New Mexico during the early stages of glacial advance, but, as discussed in Section D, the wettest climate did not occur until the continental ice sheet reached its greatest extent approximately 20,000 years ago (Swift, 1993). Climatic changes near the

WIPP early in a glacial period, before the full growth of the continental ice sheet and the consequent disruption and southward shift of the jet stream, would presumably be less extreme than those of the glacial maximum. Based on these observations, we believe the step recharge function, which represents a radical disruption of the climatic pattern of the Holocene, is relatively unlikely, and we assign it a 0.25 probability of occurrence.

Mechanisms that produce the climatic variability observed in the Holocene are not well understood, but fluctuations analogous to those seen in the precipitation record for southeastern New Mexico (Swift, 1993) are also observed in Greenland ice cores (O'Brien et al., 1995). Solar variability, changes in oceanic circulation patterns, and volcanic activity are all proposed as factors that may have influenced Holocene climatic fluctuations (Stuiver et al., 1995). Causal relationships between these factors and precipitation at the WIPP are not proposed here, and we do not believe it is useful for this purpose to attempt direct prediction of future climate changes. However, based on the observation that there is no basis for assuming that the frequency of any natural factors influencing Holocene climatic variability will change in the next 10,000 years, we believe that it is reasonable to assume that such changes will continue to occur. The Holocene recharge pattern is therefore assigned a 0.75 probability of occurrence.

Effects on Groundwater Flow

In the previous section we presented the rationale for assigning a 0.75 probability to a continuation of the Holocene pattern of recharge to the future and a 0.25 probability to a future recharge pattern that is represented by the step pattern. The objective of this section is to present the rationale for the distribution of the Climate Index for each of the two future recharge patterns.

FUTURE REPRESENTED BY THE STEP RECHARGE FUNCTION

Simulations using the step recharge function for the future show a smooth increase in heads and lateral flow rates in the future. Consequently the lateral-flow ratio reaches its maximum value at the end of the simulation (at 10,000 years). We use this value to represent the future change in lateral flow rates in these simulations.

We first consider the uncertainty in the maximum Holocene recharge rate. Two sets of simulations address this uncertainty. Each set has fixed hydraulic properties and contains simulations assuming values of maximum Holocene recharge of 0.2, 0.4, and 0.6 mm/yr. The first set consists of simulations 30, 37, and 38. The lateral-flow ratios for these simulations are 1.6, 1.7, and 1.6. These ratios show little sensitivity to the maximum rate of Holocene recharge. The second set of simulations, numbers 32, 39, and 40, have lateral-flow ratios of 1.6, 2.1, and 2.1. These simulations show larger ratios for maximum recharge rates of 0.4 and 0.6 mm/yr. The range of values for the lateral-flow ratios for these six simulations is 1.6 to 2.1. In order to reflect what we believe is an appropriate level of resolution for these results, we use 0.25 as the smallest increment of the lateral-flow ratio when specifying its probability distribution. We tentatively assign a distribution ranging from 1.5 to 2.25 with equal probability of all values.

The six simulations on which we have based the tentative distribution consider only two sets of hydraulic properties. We next examine results from a series of 7 simulations (numbers 30, through 36) in which the maximum Holocene recharge is fixed at 0.2 mm/yr but the hydraulic properties are different in each case. The hydraulic properties of the sets were selected to represent an extensive range of possible hydrologic responses. As shown in Table 8, the lateral-flow ratios for these simulations are, in the order of the simulation numbers, 1.6, 1.2, 1.6, 2.0, 1.4, 1.4, and 1.0. These results suggest that the range of lateral-flow ratios is not altered very much if a larger range of hydraulic properties is considered. If anything, these results suggest that the lower limit of the range should be decreased from 1.5 to 1.0. We choose not to alter the tentative distribution to reflect this larger range.

Finally, there are 12 pairs of steady-state simulations that provide additional information about the sensitivity of the lateral-flow ratio to the choice of hydraulic properties. These are the pairs, 2/29, 3/30, 5/32, 6/33, 11/38, 12/39, 14/41, 15/42, 20/47, 21/48, 23/50, and 24/51. The other 15 pairs of steady-state simulations listed in Table 4 have an anhydrite conductivity of 1×10^{-11} and/or a conductivity of 2×10^{-6} m/s for the Dewey lake/Triassic rocks. As noted above, these choices of rock properties result in unrealistically small vertical gradients of head and are therefore not considered to be representative. The lateral-flow ratios for the 12 representative pairs are, in the order listed, 1.4, 1.5, 1.8, 1.1, 1.1, 1.0, 1.1, 1.0, 0.9, 0.7, 1.0, and 0.8. Using a rationale similar to that for the transient simulations for various hydraulic properties, we choose not to modify the tentative distribution for the Climate Index for the step pattern used for future recharge. Therefore, this distribution remains as being uniform between 1.5 and 2.25.

FUTURE REPRESENTED BY THE HOLOCENE RECHARGE FUNCTION

There are 6 transient simulations (numbers 41 through 46) that use the Holocene pattern of future recharge. These differ from simulations (numbers 30, 37, 38, 32, 39, 40) used to determine the Climate Index for the future step recharge function only in the pattern of future recharge; the hydraulic properties and the maximum Holocene recharge rates are the same as in the corresponding simulations.

The Holocene pattern of future recharge results in periodic increases and decreases of future heads and lateral flow rates that correspond to future wet and dry periods. Consequently, the lateral-flow ratio at the end of the simulation is not representative. Instead, of using a value of this ratio at a single time, we have calculated a continuous record of the lateral-flow ratio from the present time until 10,000 years in the future. These records are shown in Figure 10. As discussed above, the lateral-flow ratio is dominated by the effects of wet periods if the Holocene recharge function is assumed. Presumably, future transport of radionuclides in the Culebra would be slightly faster during those time in which lateral flow is faster. Although, these results suggest that a representative future lateral-flow ratio could be as low as 0.9, we will assume 1.0 as the lower range in the specified distribution. We specify a distribution ranging from 1.0 to 1.25 with equal probability of all values for the Holocene recharge function.

G. References

- Bear, J. and A. Verruijt, 1987. *Modeling Groundwater Flow and Pollution*, D. Reidel Pub. Co., Dordrecht.
- Campbell, A. R., F. M. Phillips, and R. J. Vanlandingham, 1996. Stable isotope study of soil water, WIPP site New Mexico: estimation of recharge to Rustler aquifers. *Radioactive Waste Management and Environmental Restoration*, v. 20, p. 153-165.
- COHMAP (Cooperative Holocene Mapping Project) Members. 1988. "Climatic Changes of the Last 18,000 Years: Observations and Model Simulations," *Science* v. 241, 1043-1052.
- Dagan, G., 1989. *Flow and Transport in Porous Formations*, Springer-Verlag, New York.
- Dansgaard, W., S.J. Johnsen, H.B. Clausen, D. Dahl-Jensen, N.S. Gundestrup, C.U. Hammer, C.S. Hvidberg, J.P. Steffensen, A.E. Sveinbjornsdottir, J. Jouzel, and G. Bond. 1993. "Evidence for general instability of past climate from a 250-kyr ice-core record," *Nature* v. 364, 218-220.
- Freeze, R.A., and J.A. Cherry. 1979. *Groundwater*. Englewood Cliffs, NJ: Prentice-Hall.
- Freeze, R.A., and P.A. Witherspoon. 1967. "Theoretical Analyses of Regional Ground Water Flow: 2. Effect of Water Table Configuration and Subsurface Permeability Variation," *Water Resources Research*. Vol. 3, 623-634.
- Hays, J.D., J. Imbrie, and N.J. Shackleton. 1976. "Variations in the Earth's orbit: pacemaker of the Ice Ages," *Science* v. 194, 1121-1132.
- Houghton, J.T., G.J. Jenkins, and J.J. Ephraums. 1990. *Climate Change: The IPCC Scientific Assessment*. Cambridge University Press, New York, NY.
- Hubbert, M.K. 1940. "The Theory of Ground-Water Motion," *The Journal of Geology*. Vol. 48, no. 8, pt. 1, 785-944.
- Imbrie, J. 1985. "A theoretical framework for the Pleistocene Ice Ages," *Journal of the Geological Society* v. 142:417-432.
- Imbrie, J., and J.Z. Imbrie. 1980. "Modeling the climatic response to orbital variations," *Science* v. 207, 943-953.
- Imbrie, J., J.D. Hays, D.G. Martinson, A. McIntyre, A.C. Mix, J.J. Morley, N.G. Pisias, W.L. Prell, and J.J. Shackleton. 1984. The orbital theory of Pleistocene climate: support from a

revised chronology of the marine $\delta^{18}\text{O}$ record, pp. 269-305, Part 1. In: *Milankovitch and Climate, Proceedings of the NATO Advanced Research Workshop on Milankovitch, Palisades, NY, November 30-December 4, 1982*. A.L. Berger, J. Imbrie, J. Hays, G. Kukla, and B. Saltzman (eds.). D. Reidel Publishing Co., Boston MA.

Knupp, P., 1996. A moving mesh algorithm for 3-D regional groundwater flow with water table and seepage face. *Advances in Water Resources*, v. 19, n. 2, p. 83-95.

Marsily, G. de., 1986. *Quantitative Hydrogeology*, Academic Press, San Diego, CA.

Milankovitch, M. 1941. *Canon of Insolation and the Ice-Age Problem*. Koniglich Serbische Akademie, Beograd. (English translation by the Israel Program for Scientific Translations; published the United States Department of Commerce and the National Science Foundation, Washington, D.C.).

Mitchell, J.F.B. 1989. "The "Greenhouse Effect" and climate change" *Reviews of Geophysics* v. 27, 115-139.

O'Brien, S.R., P.A. Mayewski, L.D. Meeker, D.A. Meese, M.S. Twickler, S.I. Whitlow. 1995. "Complexity of Holocene Climate as Reconstructed from a Greenland Ice Core," *Science* v. 270, 1962-1964.

Powers, D.W., and R.M. Holt. 1990. "Sedimentology of the Rustler Formation near the Waste Isolation Pilot Plant (WIPP) Site," *Geological and Hydrological Studies of Evaporites in the Northern Delaware Basin for the Waste Isolation Pilot Plant (WIPP), New Mexico, Field Trip #14 Guidebook, Geological Society of America 1990 Annual Meeting, Dallas, TX, October 29-November 1, 1990*. Leaders: D.W. Powers, R.M. Holt, R.L. Beauheim, and N. Rempe. Dallas, TX: Dallas Geological Society. 79-106.

Raynaud, D., J. Jouzel, J.M. Barnola, J. Chappellaz, R.J. Delmas, and C. Lorius. 1993. "The Ice Record of Greenhouse Gases," *Science* v. 259, 926-934.

Schlesinger, M.E., and J.F.B. Mitchell. 1987. "Climate model simulations of the equilibrium climatic response to increased carbon dioxide," *Reviews of Geophysics* v. 25, 760-798.

Stuiver, M., P.M. Grootes, and T.F. Braziunas. 1995. "The GISP2 $\delta^{18}\text{O}$ Climate Record of the Past 16,500 Years and the Role of the Sun, Ocean, and Volcanoes," *Quaternary Research* v. 44, 341-354.

Swift, P. N. 1993. Long-term climate variability at the Waste Isolation Pilot Plant, southeastern New Mexico, USA. *Environmental Management*, v. 17. P. 83-97.

Tóth, J. 1963. "A Theoretical Analysis of Groundwater Flow in Small Drainage Basins," *Journal*

of Geophysical Research. Vol. 68, no. 16, 4795-4812.

US EPA (United States Environmental Protection Agency). 1996. "Criteria for the Certification and Re-Certification of the Waste Isolation Pilot Plant's Compliance With the 40 CFR Part 191 Disposal Regulations; Final Rule," *Federal Register* v. 61, 5224-5245.

Washington, W.M., and G.A. Meehl. 1984. "Seasonal cycle experiment on the climate sensitivity due to doubling of CO₂ with an atmospheric general circulation model coupled to a simple mixed-layer ocean model" *Journal of Geophysical Research* v. 89, 9475-9503.

Wilson, C.A., and J.F.B. Mitchell. 1987. "A doubled CO₂ climate sensitivity experiment with a global climate model including a simple ocean," *Journal of Geophysical Research* v. 92, 13,315-13,343.

Table 1. Values of intact hydraulic conductivity (K in m/s) for steady-state simulations.

| simulation* | K disrupted region | K anhydrite | K Dewey Lake | K Culebra | K Magenta | K halite | K mudstone |
|-------------|----------------------|---------------------|--------------------|----------------------|----------------------|---------------------|--------------------|
| 1, 28 | $1 \times 10^{-4.5}$ | 1×10^{-13} | 2×10^{-6} | $1 \times 10^{-7.5}$ | $1 \times 10^{-8.5}$ | 1×10^{-13} | 1×10^{-9} |
| 2, 29 | $1 \times 10^{-4.5}$ | 1×10^{-13} | 2×10^{-7} | $1 \times 10^{-7.5}$ | $1 \times 10^{-8.5}$ | 1×10^{-13} | 1×10^{-9} |
| 3, 30 | $1 \times 10^{-4.5}$ | 1×10^{-13} | 2×10^{-8} | $1 \times 10^{-7.5}$ | $1 \times 10^{-8.5}$ | 1×10^{-13} | 1×10^{-9} |
| 4, 31 | $1 \times 10^{-4.5}$ | 1×10^{-12} | 2×10^{-6} | $1 \times 10^{-7.5}$ | $1 \times 10^{-8.5}$ | 1×10^{-13} | 1×10^{-9} |
| 5, 32 | $1 \times 10^{-4.5}$ | 1×10^{-12} | 2×10^{-7} | $1 \times 10^{-7.5}$ | $1 \times 10^{-8.5}$ | 1×10^{-13} | 1×10^{-9} |
| 6, 33 | $1 \times 10^{-4.5}$ | 1×10^{-12} | 2×10^{-8} | $1 \times 10^{-7.5}$ | $1 \times 10^{-8.5}$ | 1×10^{-13} | 1×10^{-9} |
| 7, 34 | $1 \times 10^{-4.5}$ | 1×10^{-11} | 2×10^{-6} | $1 \times 10^{-7.5}$ | $1 \times 10^{-8.5}$ | 1×10^{-13} | 1×10^{-9} |
| 8, 35 | $1 \times 10^{-4.5}$ | 1×10^{-11} | 2×10^{-7} | $1 \times 10^{-7.5}$ | $1 \times 10^{-8.5}$ | 1×10^{-13} | 1×10^{-9} |
| 9, 36 | $1 \times 10^{-4.5}$ | 1×10^{-11} | 2×10^{-8} | $1 \times 10^{-7.5}$ | $1 \times 10^{-8.5}$ | 1×10^{-13} | 1×10^{-9} |
| 10, 37 | $1 \times 10^{-5.5}$ | 1×10^{-13} | 2×10^{-6} | $1 \times 10^{-7.5}$ | $1 \times 10^{-8.5}$ | 1×10^{-13} | 1×10^{-9} |
| 11, 38 | $1 \times 10^{-5.5}$ | 1×10^{-13} | 2×10^{-7} | $1 \times 10^{-7.5}$ | $1 \times 10^{-8.5}$ | 1×10^{-13} | 1×10^{-9} |
| 12, 39 | $1 \times 10^{-5.5}$ | 1×10^{-13} | 2×10^{-8} | $1 \times 10^{-7.5}$ | $1 \times 10^{-8.5}$ | 1×10^{-13} | 1×10^{-9} |
| 13, 40 | $1 \times 10^{-5.5}$ | 1×10^{-12} | 2×10^{-6} | $1 \times 10^{-7.5}$ | $1 \times 10^{-8.5}$ | 1×10^{-13} | 1×10^{-9} |
| 14, 41 | $1 \times 10^{-5.5}$ | 1×10^{-12} | 2×10^{-7} | $1 \times 10^{-7.5}$ | $1 \times 10^{-8.5}$ | 1×10^{-13} | 1×10^{-9} |
| 15, 42 | $1 \times 10^{-5.5}$ | 1×10^{-12} | 2×10^{-8} | $1 \times 10^{-7.5}$ | $1 \times 10^{-8.5}$ | 1×10^{-13} | 1×10^{-9} |
| 16, 43 | $1 \times 10^{-5.5}$ | 1×10^{-11} | 2×10^{-6} | $1 \times 10^{-7.5}$ | $1 \times 10^{-8.5}$ | 1×10^{-13} | 1×10^{-9} |

| | | | | | | | |
|--------|----------------------|---------------------|--------------------|----------------------|----------------------|---------------------|--------------------|
| 17, 44 | $1 \times 10^{-5.5}$ | 1×10^{-11} | 2×10^{-7} | $1 \times 10^{-7.5}$ | $1 \times 10^{-8.5}$ | 1×10^{-13} | 1×10^{-9} |
| 18, 45 | $1 \times 10^{-5.5}$ | 1×10^{-11} | 2×10^{-8} | $1 \times 10^{-7.5}$ | $1 \times 10^{-8.5}$ | 1×10^{-13} | 1×10^{-9} |
| 19, 46 | $1 \times 10^{-6.5}$ | 1×10^{-13} | 2×10^{-6} | $1 \times 10^{-7.5}$ | $1 \times 10^{-8.5}$ | 1×10^{-13} | 1×10^{-9} |
| 20, 47 | $1 \times 10^{-6.5}$ | 1×10^{-13} | 2×10^{-7} | $1 \times 10^{-7.5}$ | $1 \times 10^{-8.5}$ | 1×10^{-13} | 1×10^{-9} |
| 21, 48 | $1 \times 10^{-6.5}$ | 1×10^{-13} | 2×10^{-8} | $1 \times 10^{-7.5}$ | $1 \times 10^{-8.5}$ | 1×10^{-13} | 1×10^{-9} |
| 22, 49 | $1 \times 10^{-6.5}$ | 1×10^{-12} | 2×10^{-6} | $1 \times 10^{-7.5}$ | $1 \times 10^{-8.5}$ | 1×10^{-13} | 1×10^{-9} |
| 23, 50 | $1 \times 10^{-6.5}$ | 1×10^{-12} | 2×10^{-7} | $1 \times 10^{-7.5}$ | $1 \times 10^{-8.5}$ | 1×10^{-13} | 1×10^{-9} |
| 24, 51 | $1 \times 10^{-6.5}$ | 1×10^{-12} | 2×10^{-8} | $1 \times 10^{-7.5}$ | $1 \times 10^{-8.5}$ | 1×10^{-13} | 1×10^{-9} |
| 25, 52 | $1 \times 10^{-6.5}$ | 1×10^{-11} | 2×10^{-6} | $1 \times 10^{-7.5}$ | $1 \times 10^{-8.5}$ | 1×10^{-13} | 1×10^{-9} |
| 26, 53 | $1 \times 10^{-6.5}$ | 1×10^{-11} | 2×10^{-7} | $1 \times 10^{-7.5}$ | $1 \times 10^{-8.5}$ | 1×10^{-13} | 1×10^{-9} |
| 27, 54 | $1 \times 10^{-6.5}$ | 1×10^{-11} | 2×10^{-8} | $1 \times 10^{-7.5}$ | $1 \times 10^{-8.5}$ | 1×10^{-13} | 1×10^{-9} |

* the numbers used for transient and steady-state simulations overlap; the text always makes it clear which is being referred to.

Table 2. Values of hydraulic conductivity (K in m/s) and specific yield for the transient simulations.

| simulation* | K disturbed | K anhydrite | K Dewey Lake | K Culebra | K Magenta | K halite | K mudstone | Specific Yield |
|-------------------|----------------------|---------------------|--------------------|----------------------|----------------------|---------------------|--------------------|----------------|
| 30,37,38,41,42,43 | $1 \times 10^{-5.5}$ | 1×10^{-12} | 2×10^{-7} | $1 \times 10^{-7.5}$ | $1 \times 10^{-8.5}$ | 1×10^{-13} | 1×10^{-9} | 0.01 |
| 31 | $1 \times 10^{-5.5}$ | 1×10^{-13} | 2×10^{-7} | $1 \times 10^{-7.5}$ | $1 \times 10^{-8.5}$ | 1×10^{-13} | 1×10^{-9} | 0.01 |
| 32,39,40,44,45,46 | $1 \times 10^{-4.5}$ | 1×10^{-12} | 2×10^{-7} | $1 \times 10^{-7.5}$ | $1 \times 10^{-8.5}$ | 1×10^{-13} | 1×10^{-9} | 0.01 |
| 33 | $1 \times 10^{-5.5}$ | 1×10^{-12} | 1×10^{-6} | $1 \times 10^{-7.5}$ | $1 \times 10^{-8.5}$ | 1×10^{-13} | 1×10^{-9} | 0.01 |
| 34 | $1 \times 10^{-5.5}$ | 1×10^{-12} | 2×10^{-7} | $1 \times 10^{-6.5}$ | $1 \times 10^{-8.5}$ | 1×10^{-13} | 1×10^{-9} | 0.01 |
| 35 | $1 \times 10^{-5.5}$ | 1×10^{-12} | 2×10^{-7} | $1 \times 10^{-7.5}$ | $1 \times 10^{-7.5}$ | 1×10^{-13} | 1×10^{-9} | 0.01 |
| 36 | $1 \times 10^{-5.5}$ | 1×10^{-12} | 2×10^{-7} | $1 \times 10^{-7.5}$ | $1 \times 10^{-8.5}$ | 1×10^{-13} | 1×10^{-9} | 0.05 |

* the numbers used for transient and steady-state simulations overlap; the text always makes it clear which is being referred to:

Table 3. Rates of potential recharge used for the transient simulations.

| simulation | Late Pleistocene recharge (mm/yr) | Holocene minimum recharge (mm/yr) | Holocene peak recharge (mm/yr) | Recharge pattern |
|---------------|-----------------------------------|-----------------------------------|--------------------------------|------------------|
| 30 through 36 | 2.0 | 0.0 | 0.2 | step |
| 41,44 | 2.0 | 0.0 | 0.2 | Holocene |
| 37,39 | 2.0 | 0.0 | 0.4 | step |
| 42,45 | 2.0 | 0.0 | 0.4 | Holocene |
| 38,40 | 2.0 | 0.0 | 0.6 | step |
| 43,46 | 2.0 | 0.0 | 0.6 | Holocene |

Table 4. Mass balance over the Culebra reference volume for the steady-state simulations.

| simulation | total flow (m ³ /yr) | % in top | % in base | % in sides | % out top | % out base | % out sides |
|------------|------------------------------------|-------------|--------------|---------------|--------------|---------------|----------------|
| 1 | 1076 | 2.5 | 0.4 | 97.0 | 0.0 | 0.8 | 99.2 |
| 2 | 2141 | 6.4 | 1.9 | 91.7 | 0.0 | 0.3 | 99.7 |
| 3 | 2074 | 12.7 | 3.9 | 83.5 | 0.0 | 0.0 | 100.0 |
| 4 | 1550 | 25.3 | 0.6 | 74.2 | 0.0 | 0.8 | 99.2 |
| 5 | 2441 | 67.2 | 2.6 | 30.2 | 0.0 | 0.8 | 99.2 |
| 6 | 3793 | 86.9 | 4.0 | 9.1 | 0.0 | 0.9 | 99.1 |
| 7 | 1413 | 21.4 | 0.3 | 78.4 | 9.3 | 0.9 | 89.9 |
| 8 | 6667 | 97.8 | 1.2 | 1.0 | 0.0 | 1.4 | 98.6 |
| 9 | 13136 | 96.4 | 1.6 | 2.0 | 0.0 | 1.4 | 98.6 |
| 10 | 1239 | 1.4 | 0.5 | 98.1 | 0.0 | 0.8 | 99.2 |
| 11 | 2729 | 4.2 | 1.7 | 94.0 | 0.0 | 0.5 | 99.5 |
| 12 | 3225 | 6.4 | 2.4 | 91.2 | 0.0 | 0.3 | 99.7 |
| 13 | 1613 | 13.9 | 0.5 | 85.5 | 0.0 | 0.8 | 99.2 |
| 14 | 3819 | 35.6 | 1.4 | 63.0 | 0.0 | 0.4 | 99.6 |
| 15 | 4595 | 54.7 | 2.7 | 42.6 | 0.0 | 0.5 | 99.5 |
| 16 | 2024 | 44.5 | 0.5 | 55.0 | 3.0 | 1.0 | 96.0 |
| 17 | 6294 | 79.9 | 1.0 | 19.1 | 0.0 | 1.1 | 98.9 |
| 18 | 10647 | 95.2 | 1.5 | 3.2 | 0.0 | 1.4 | 98.6 |
| 19 | 1594 | 1.6 | 0.9 | 97.5 | 0.0 | 0.7 | 99.3 |
| 20 | 2720 | 3.9 | 1.7 | 94.4 | 0.0 | 0.3 | 99.7 |
| 21 | 3125 | 5.6 | 2.3 | 92.1 | 0.0 | 0.1 | 99.9 |
| 22 | 1709 | 12.6 | 0.8 | 86.6 | 0.0 | 0.6 | 99.4 |
| 23 | 3290 | 33.1 | 1.5 | 65.3 | 0.0 | 0.3 | 99.7 |

| | | | | | | | |
|----|-------|------|-----|------|-----|-----|-------|
| 24 | 4328 | 42.2 | 2.4 | 55.4 | 0.0 | 0.4 | 99.6 |
| 25 | 1759 | 41.2 | 0.5 | 58.3 | 1.7 | 0.9 | 97.4 |
| 26 | 5064 | 77.1 | 1.0 | 21.9 | 0.0 | 1.1 | 98.9 |
| 27 | 8824 | 88.2 | 1.4 | 10.4 | 0.0 | 1.2 | 98.8 |
| 28 | 2516 | 4.4 | 1.8 | 93.7 | 0.0 | 0.5 | 99.5 |
| 29 | 3031 | 6.6 | 2.5 | 91.0 | 0.0 | 0.2 | 99.8 |
| 30 | 3132 | 7.0 | 2.5 | 90.5 | 0.0 | 0.1 | 99.9 |
| 31 | 3471 | 42.1 | 1.7 | 56.2 | 0.0 | 0.4 | 99.6 |
| 32 | 4447 | 56.8 | 2.8 | 40.4 | 0.0 | 0.5 | 99.5 |
| 33 | 4303 | 63.5 | 3.2 | 33.3 | 0.0 | 0.6 | 99.4 |
| 34 | 7055 | 97.4 | 1.1 | 1.5 | 0.0 | 1.3 | 98.7 |
| 35 | 13270 | 97.3 | 1.2 | 1.5 | 0.0 | 1.2 | 98.8 |
| 36 | 14564 | 97.3 | 1.2 | 1.5 | 0.0 | 1.2 | 98.8 |
| 37 | 2642 | 3.8 | 1.8 | 94.5 | 0.0 | 0.3 | 99.7 |
| 38 | 2969 | 5.5 | 2.3 | 92.2 | 0.0 | 0.1 | 99.9 |
| 39 | 3075 | 6.1 | 2.5 | 91.4 | 0.0 | 0.2 | 99.8 |
| 40 | 3446 | 36.8 | 1.7 | 61.5 | 0.0 | 0.4 | 99.6 |
| 41 | 4309 | 45.8 | 2.6 | 51.6 | 0.0 | 0.4 | 99.6 |
| 42 | 4459 | 49.4 | 2.7 | 47.9 | 0.0 | 0.4 | 99.6 |
| 43 | 6484 | 91.5 | 1.1 | 7.4 | 0.0 | 1.2 | 98.8 |
| 44 | 9952 | 96.9 | 1.3 | 1.8 | 0.0 | 1.2 | 98.8 |
| 45 | 11087 | 97.0 | 1.2 | 1.8 | 0.0 | 1.2 | 98.8 |
| 46 | 2140 | 3.4 | 1.8 | 94.8 | 0.0 | 0.1 | 99.9 |
| 47 | 2293 | 4.4 | 2.6 | 93.0 | 0.0 | 0.0 | 100.0 |
| 48 | 2239 | 5.4 | 2.9 | 91.7 | 0.0 | 0.0 | 100.0 |
| 49 | 2742 | 32.4 | 1.9 | 65.7 | 0.0 | 0.3 | 99.7 |

Information Only

| | | | | | | | |
|----|------|------|-----|------|-----|-----|------|
| 50 | 3314 | 34.0 | 2.6 | 63.4 | 0.0 | 0.2 | 99.8 |
| 51 | 3479 | 36.4 | 2.8 | 60.8 | 0.0 | 0.2 | 99.8 |
| 52 | 4987 | 82.7 | 1.1 | 16.1 | 0.0 | 1.1 | 98.9 |
| 53 | 6301 | 87.6 | 1.4 | 11.0 | 0.0 | 1.0 | 99.0 |
| 54 | 6553 | 90.0 | 1.4 | 8.6 | 0.0 | 1.0 | 99.0 |

Table 5. Lateral-flow ratio for the steady-state simulations. Shaded values are considered to be not representative because these simulations result in unrealistic vertical gradients of head.

| simulation pair | lateral-flow ratio | simulation pair | lateral-flow ratio |
|-----------------|--------------------|-----------------|--------------------|
| 1/28 | 2.4 | 15/42 | 1.0 |
| 2/29 | 1.4 | 16/43 | 3.3 |
| 3/30 | 1.5 | 17/44 | 1.6 |
| 4/31 | 2.3 | 18/45 | 1.0 |
| 5/32 | 1.8 | 19/46 | 1.4 |
| 6/33 | 1.1 | 20/47 | 0.9 |
| 7/34 | 5.5 | 21/48 | 0.7 |
| 8/35 | 2.0 | 22/49 | 1.6 |
| 9/36 | 1.1 | 23/50 | 1.0 |
| 10/37 | 2.1 | 24/51 | 0.8 |
| 11/38 | 1.1 | 25/52 | 2.9 |
| 12/39 | 1.0 | 26/53 | 1.3 |
| 13/40 | 2.2 | 27/54 | 0.7 |
| 14/41 | 1.1 | | |

Table 6. Mass balance over the Culebra reference volume at the present time.

| simulation | flow in (m ³ /year) | | | | flow out (m ³ /year) | | | |
|------------|--------------------------------|------|-------|-------|---------------------------------|------|-------|-------|
| | top | base | sides | total | top | base | sides | total |
| 30 | 636 | 69 | 1395 | 2100 | 0 | 0 | 2107 | 2107 |
| 31 | 84 | 67 | 2017 | 2169 | 0 | 0 | 2173 | 2174 |
| 32 | 1001 | 80 | 310 | 1392 | 0 | 1 | 1396 | 1398 |
| 33 | 134 | 23 | 648 | 807 | 3 | 0 | 807 | 811 |
| 34 | 993 | 65 | 17678 | 18737 | 0 | 0 | 18744 | 18745 |
| 35 | 380 | 60 | 1676 | 2117 | 0 | 0 | 2122 | 2122 |
| 36 | 1400 | 85 | 2138 | 3625 | 0 | 7 | 3620 | 3628 |
| 37 | 798 | 87 | 1547 | 2433 | 0 | 0 | 2441 | 2441 |
| 38 | 945 | 98 | 1737 | 2781 | 0 | 0 | 2790 | 2790 |
| 39 | 1167 | 97 | 371 | 1636 | 0 | 1 | 1642 | 1644 |
| 40 | 1327 | 114 | 441 | 1882 | 0 | 1 | 1891 | 1892 |
| 41 | 636 | 69 | 1395 | 2100 | 0 | 0 | 2107 | 2107 |
| 42 | 798 | 87 | 1547 | 2433 | 0 | 0 | 2441 | 2441 |
| 43 | 945 | 98 | 1737 | 2781 | 0 | 0 | 2790 | 2790 |
| 44 | 1001 | 80 | 310 | 1392 | 0 | 1 | 1396 | 1398 |
| 45 | 1167 | 97 | 371 | 1636 | 0 | 1 | 1642 | 1644 |
| 46 | 1327 | 114 | 441 | 1882 | 0 | 1 | 1891 | 1892 |

Table 7. Mass balance over the Culebra reference volume at 10,000 years in the future.

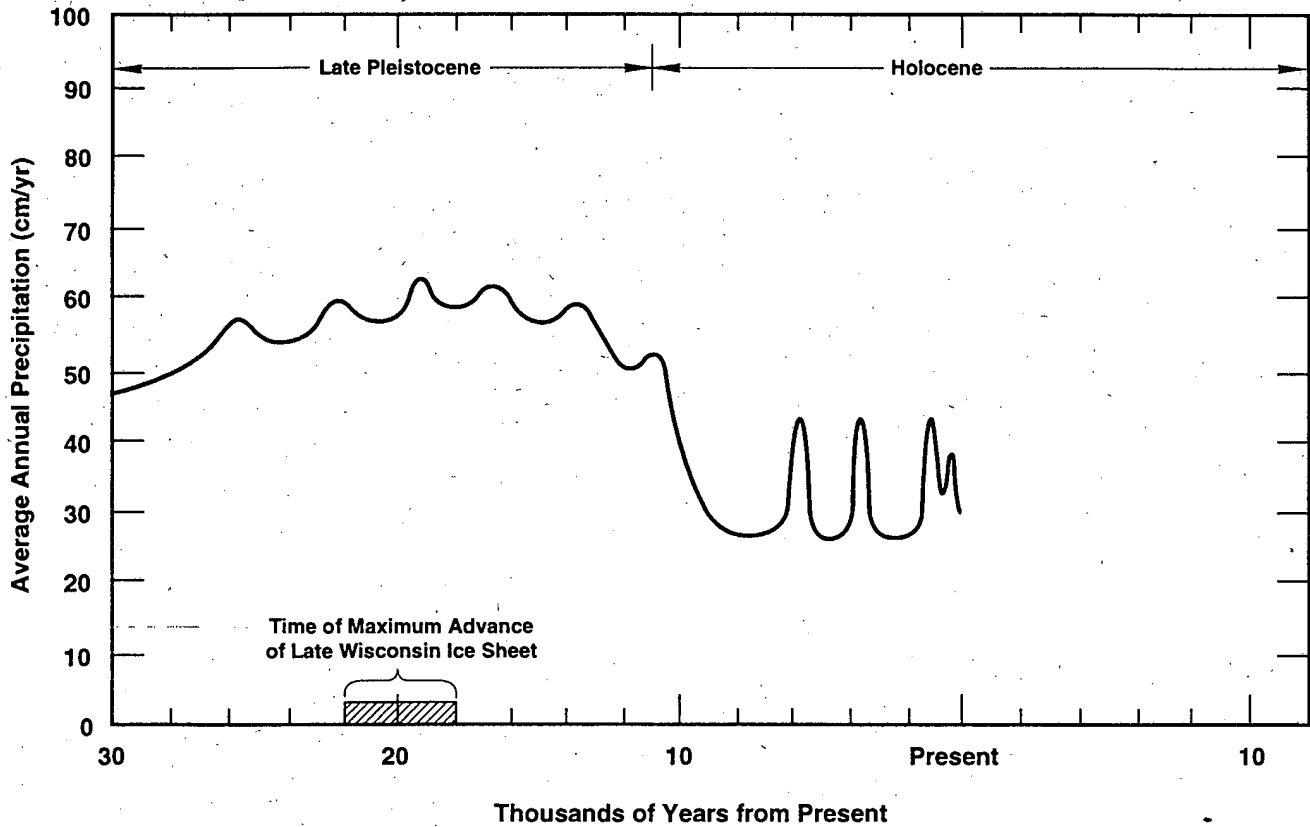
| simulation | flow in m ³ /year | | | | top | flow out (m ³ /year) | | | |
|------------|------------------------------|------|-------|-------|-----|---------------------------------|-------|-------|--|
| | top | base | sides | total | | base | sides | total | |
| 30 | 1192 | 42 | 2118 | 3354 | 0 | 17 | 3335 | 3353 | |
| 31 | 104 | 40 | 2549 | 2694 | 0 | 16 | 2677 | 2693 | |
| 32 | 1520 | 53 | 630 | 2203 | 0 | 22 | 2179 | 2202 | |
| 33 | 349 | 12 | 1259 | 1620 | 0 | 11 | 1608 | 1620 | |
| 34 | 1571 | 40 | 25417 | 27029 | 0 | 15 | 27013 | 27029 | |
| 35* | 690 | 37 | 2245 | 2973 | 0 | 11 | 2960 | 2972 | |
| 36 | 1329 | 57 | 2176 | 3564 | 0 | 12 | 3551 | 3564 | |
| 37 | 1901 | 79 | 2243 | 4224 | 0 | 21 | 4202 | 4224 | |
| 38 | 2060 | 92 | 2265 | 4418 | 0 | 20 | 4397 | 4418 | |
| 39 | 2255 | 86 | 1173 | 3515 | 0 | 30 | 3484 | 3514 | |
| 40 | 2531 | 106 | 1288 | 3926 | 0 | 28 | 3897 | 3926 | |
| 41 | 431 | 7 | 1462 | 1901 | 0 | 67 | 1820 | 1887 | |
| 42 | 675 | 7 | 1610 | 2293 | 0 | 105 | 2164 | 2269 | |
| 43 | 919 | 7 | 1992 | 2919 | 0 | 137 | 2750 | 2887 | |
| 44 | 772 | 6 | 397 | 1176 | 0 | 53 | 1110 | 1164 | |
| 45 | 999 | 5 | 505 | 1510 | 0 | 107 | 1377 | 1485 | |
| 46 | 1223 | 3 | 671 | 1898 | 0 | 163 | 1696 | 1859 | |

* This simulation ended prematurely (after about 21 cpu days). The mass balance results are given for 9,200 years in the future.

Table 8. Lateral-flow ratios at 10,000 years in the future for the transient simulations.

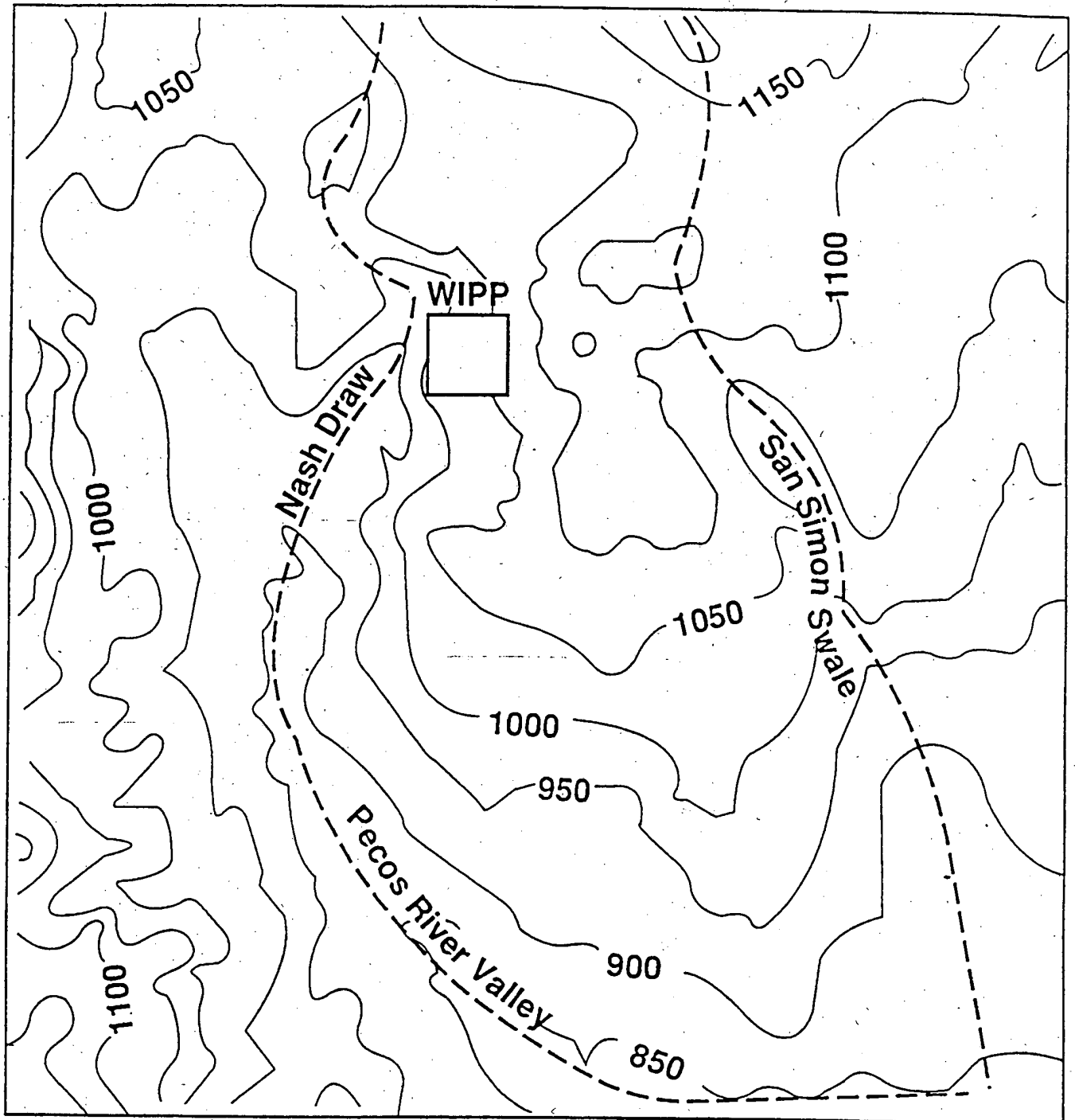
| simulation | lateral-flow ratio |
|------------|--------------------|
| 30 | 1.6 |
| 31 | 1.2 |
| 32 | 1.6 |
| 33 | 2.0 |
| 34 | 1.4 |
| 35* | 1.4 |
| 36 | 1.0 |
| 37 | 1.7 |
| 38 | 1.6 |
| 39 | 2.1 |
| 40 | 2.1 |
| 41 | 0.9 |
| 42 | 0.9 |
| 43 | 1.0 |
| 44 | 0.8 |
| 45 | 0.8 |
| 46 | 0.9 |

* This simulation ended prematurely (after about 21 cpu days). The lateral-flow ratio given is for 9,200 years in the future.



TRI-6342-5419-0

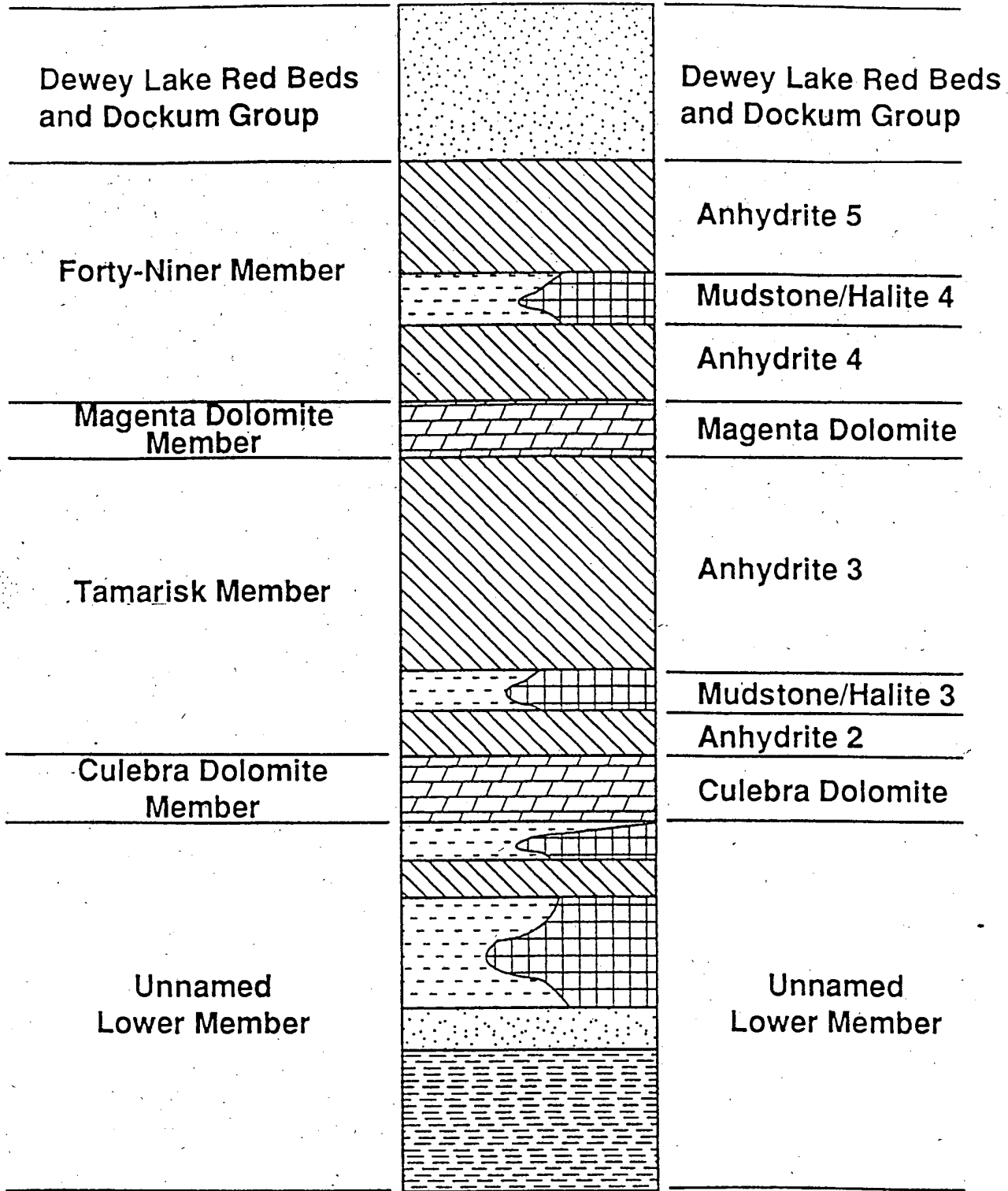
Figure 1. Estimated mean annual precipitation at the WIPP during the late Pleistocene and Holocene. (Swift, 1993).



TRI-6119-326-1

Figure 2. Outline of the numerical model domain (dashed line) on a topographic map. The contour interval is 50 meters. The model boundary follows major hydrologic divides.

Hydrostratigraphic Units



Salado Formation

Figure 3. Hydrostratigraphic units used in the numerical model. Modified from Powers and Holt (1990).

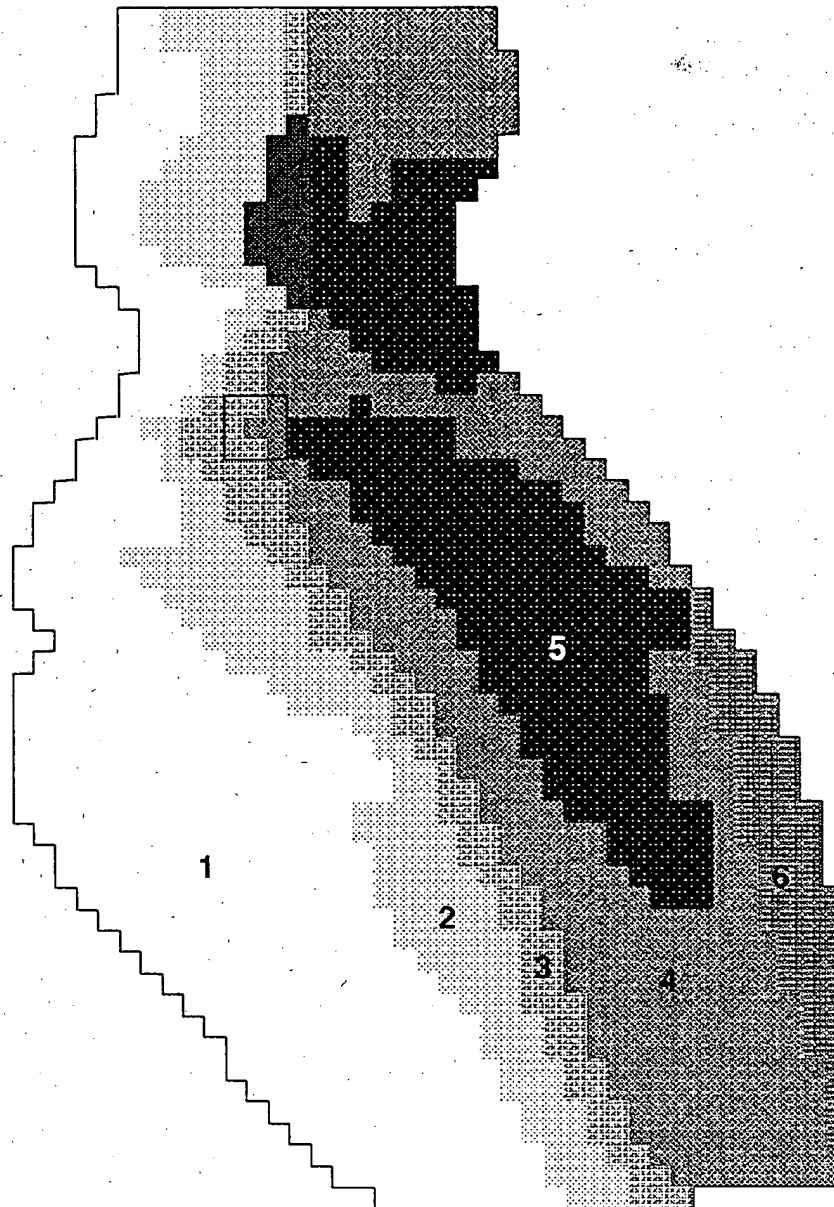


Figure 4. Zonation approach used to represent the effects of depositional setting and post-depositional processes. Zone 1 is a region in which dissolution of the upper Salado has fractured and disrupted overlying strata to the extent that stratigraphic layering is not preserved over long distances. In zone 2, dissolution of the upper Salado is thought to have fractured the Rustler, but did not disrupt layering. Fractures that predate dissolution of the upper Salado are mostly filled with gypsum. These fracture fillings have been removed in Zone 3. Zone 4 represents intact strata. The region occupied by the halite facies of the mudstone/halite layers is indicated by Zone 5. A Permian-age graben structure is shown as Zone 6.

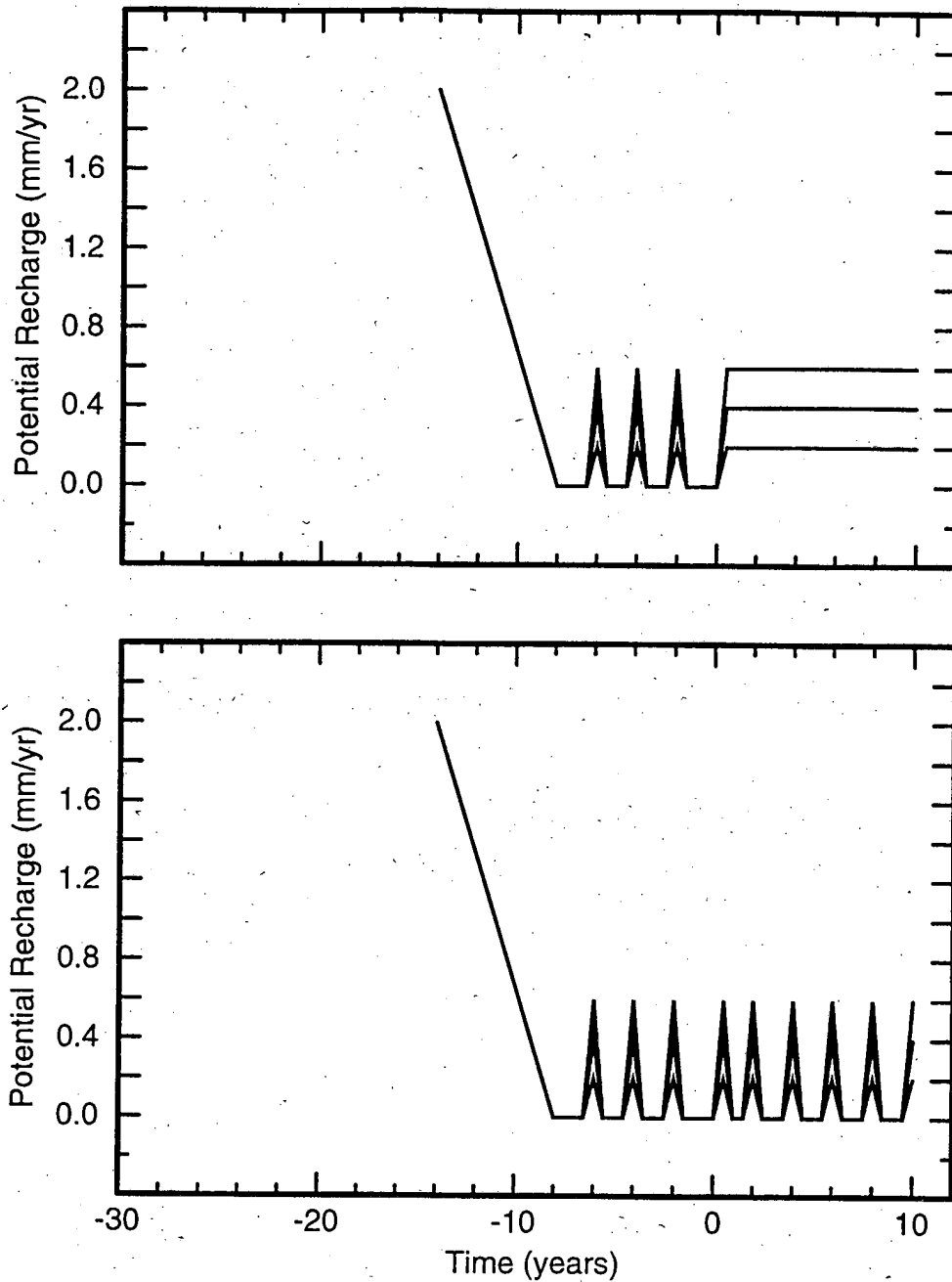


Figure 5. Assumed function for potential recharge for the transient simulations. Future recharge is represented by either the "step" pattern of recharge (top) or the "Holocene" pattern of recharge (bottom). Functions are shown for maximum Holocene recharge rates of 0.2, 0.4, and 0.6 mm/yr.

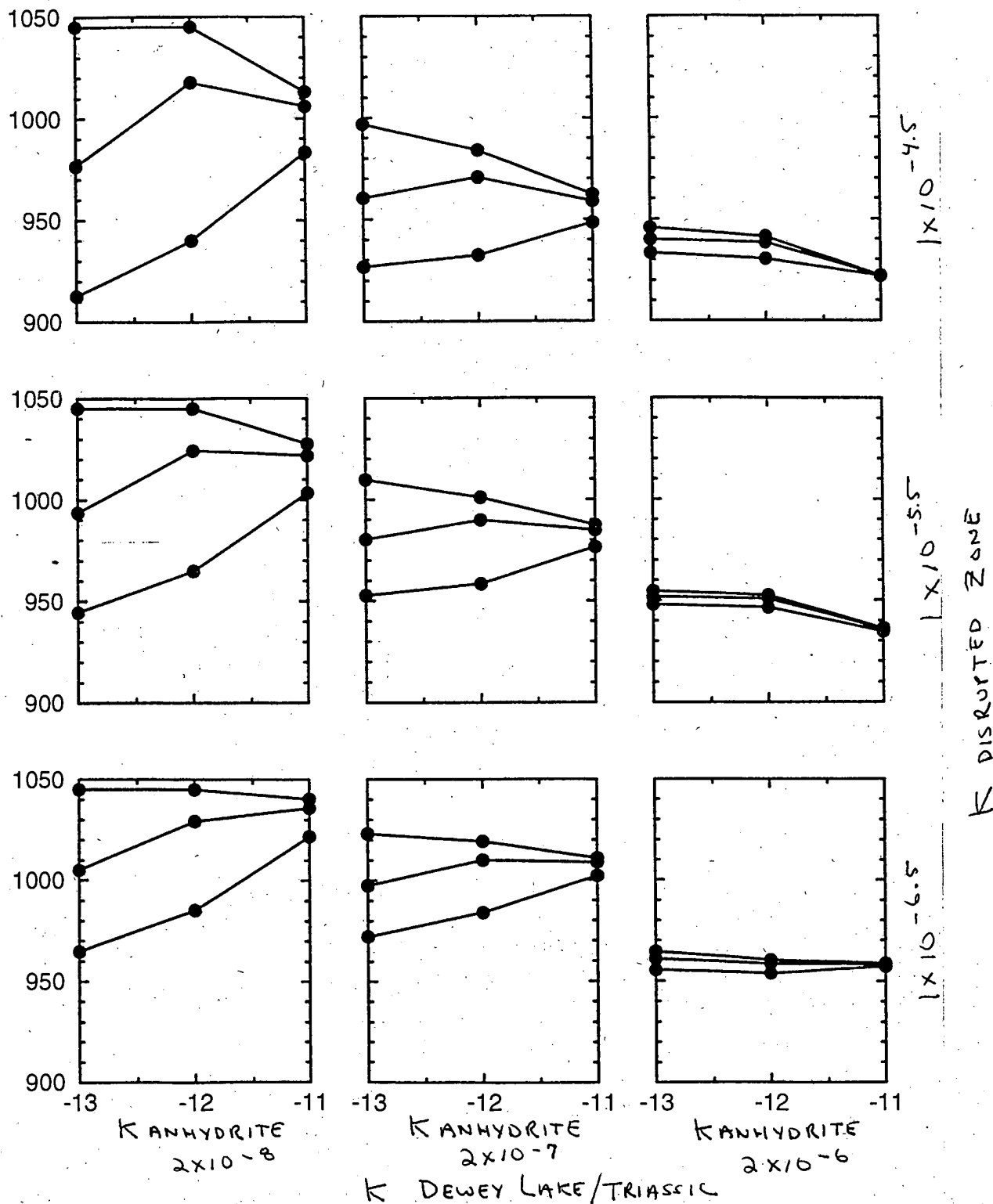


Figure 6. Simulated steady-state elevation of the water table (upper point), Magenta head, and Culebra head (lower point) near the center of the WIPP site versus the conductivity of intact anhydrite. Graphs in each row have the same value of disturbed zone conductivity and graphs in each column have the same value of conductivity of the Dewey Lake/Triassic rocks.

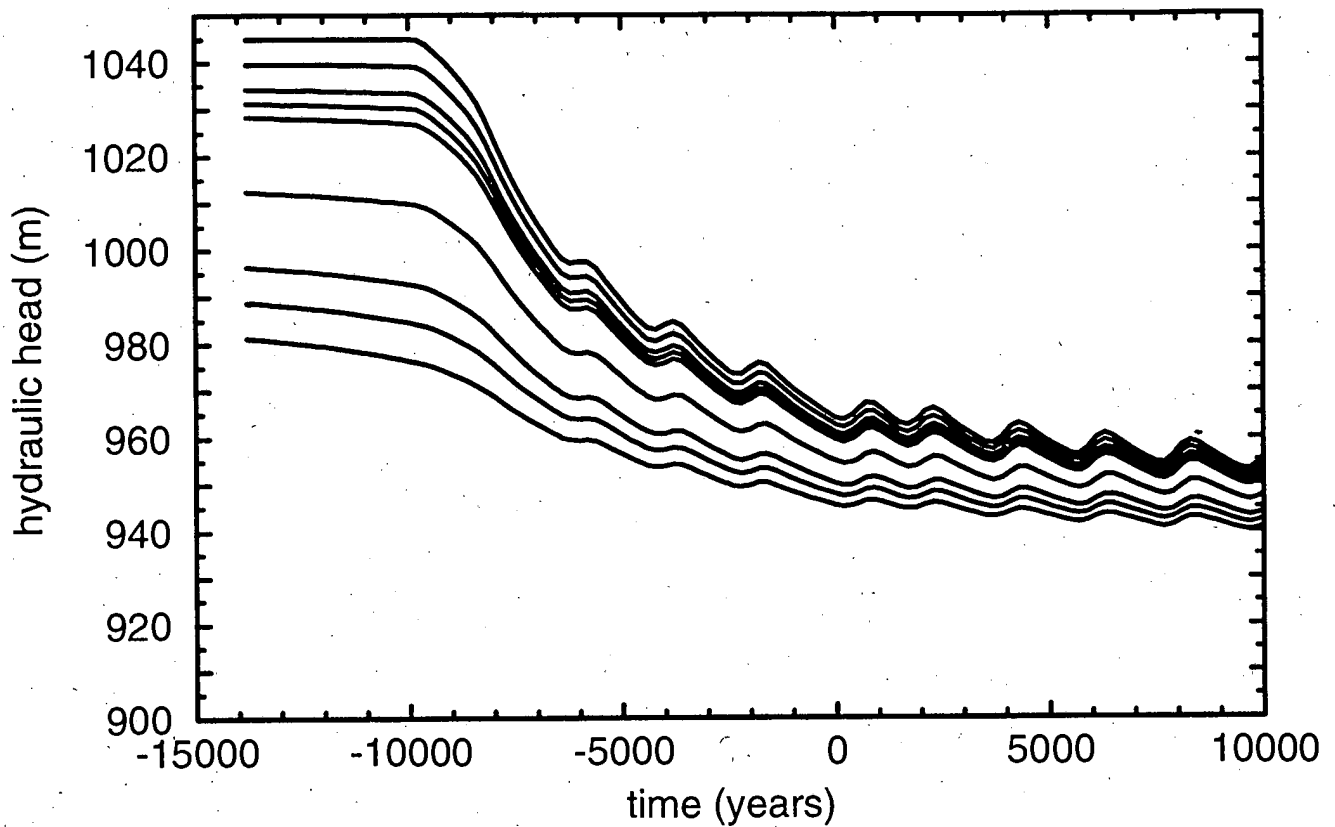
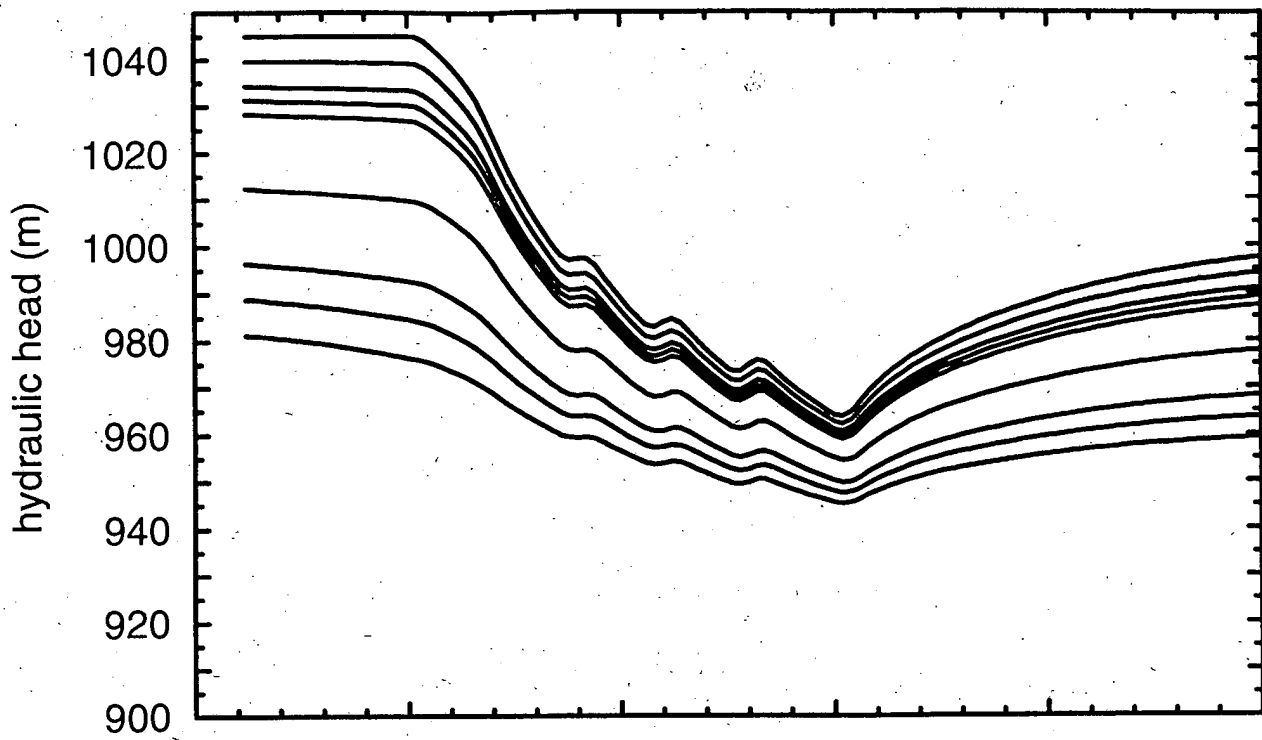


Figure 7. Elevation of the water table and head in each hydrostratigraphic unit versus time for simulations 30 (top) and 41 (bottom). The upper-most line in each graph is the water table and the lower-most line is head in the Culebra.

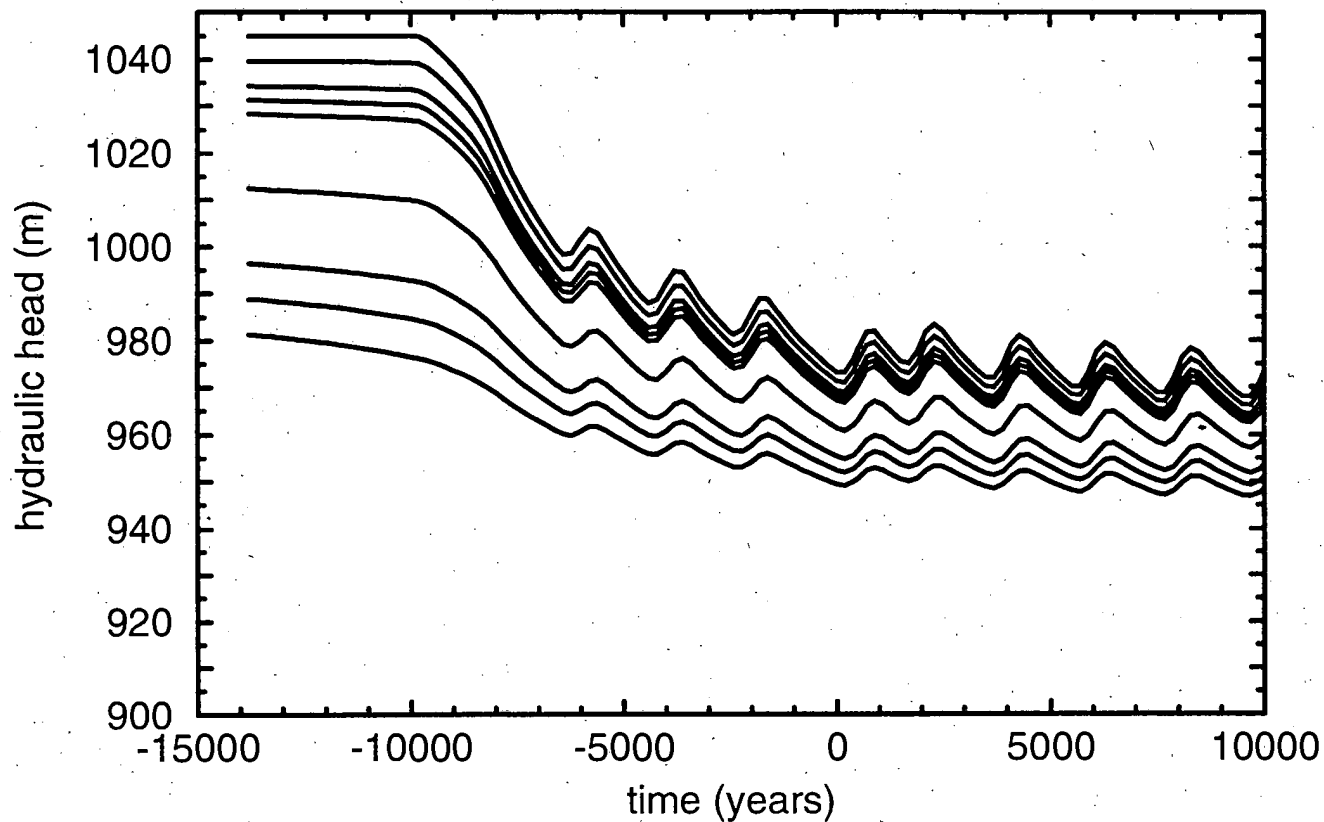
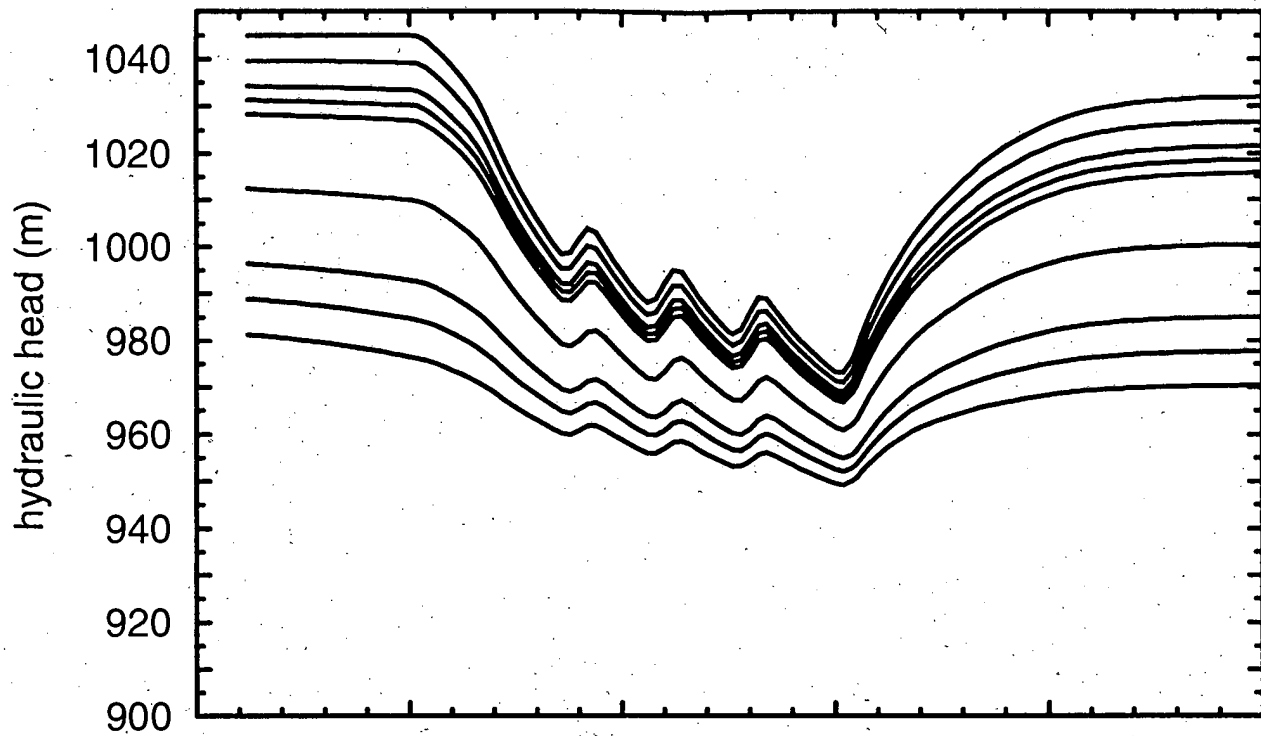


Figure 8. Elevation of the water table and head in each hydrostratigraphic unit versus time for simulations 37 (top) and 42 (bottom). The upper-most line in each graph is the water table and the lower-most line is head in the Culebra.

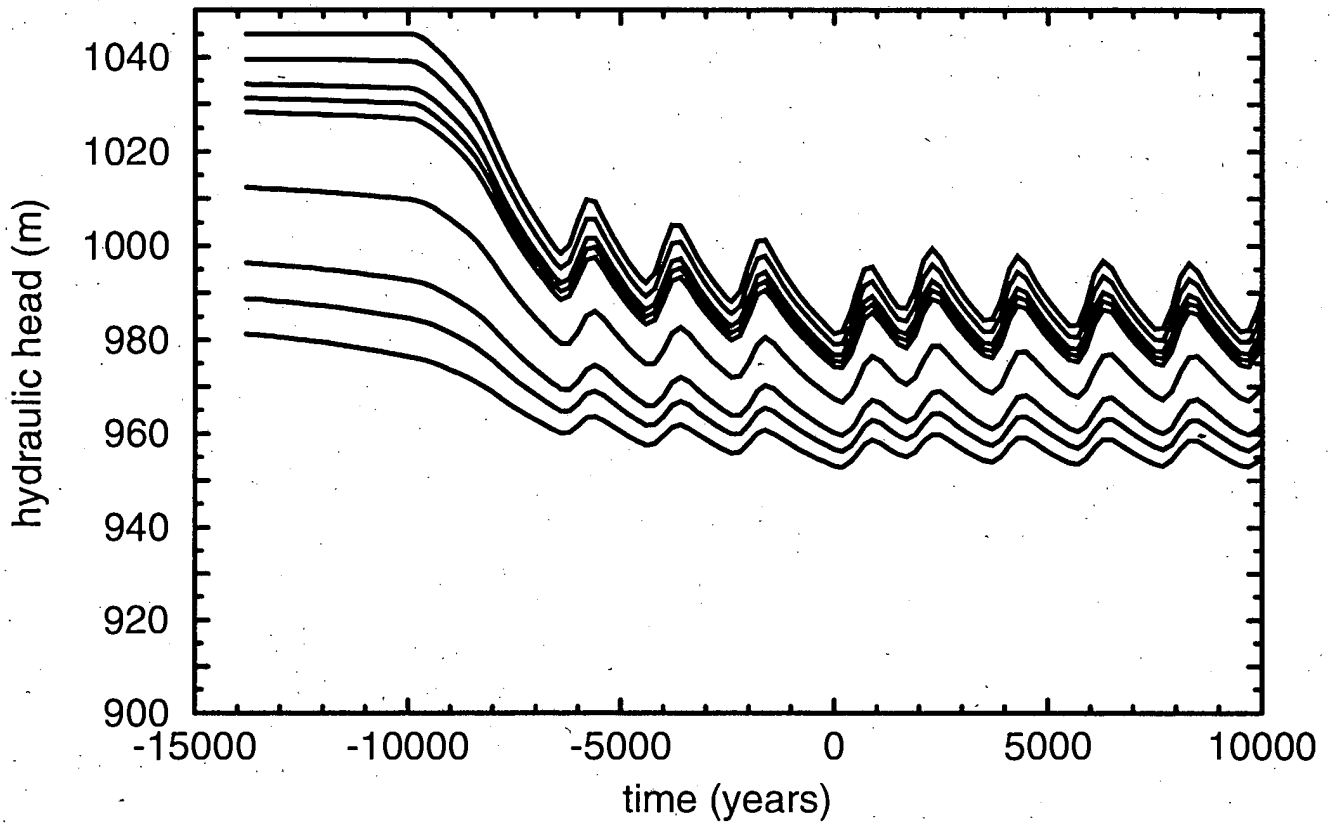
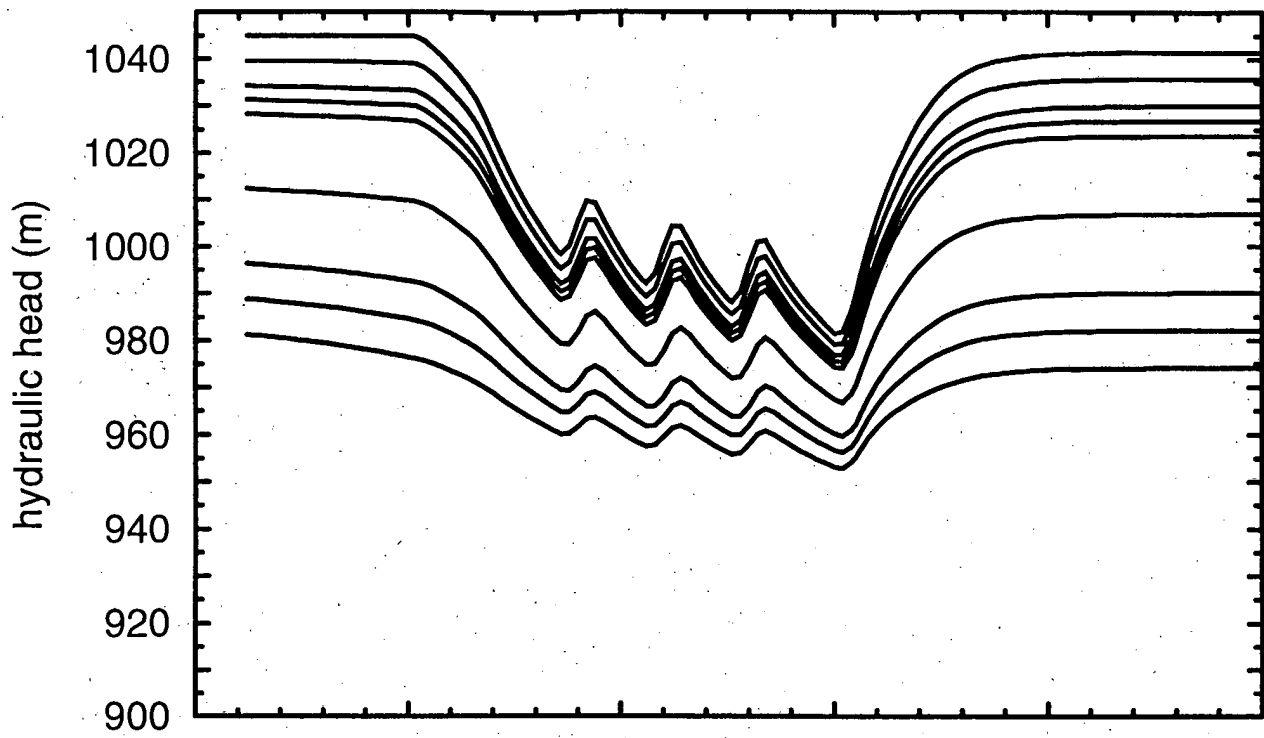


Figure 9. Elevation of the water table and head in each hydrostratigraphic unit versus time for simulations 38 (top) and 43 (bottom). The upper-most line in each graph is the water table and the lower-most line is head in the Culebra.

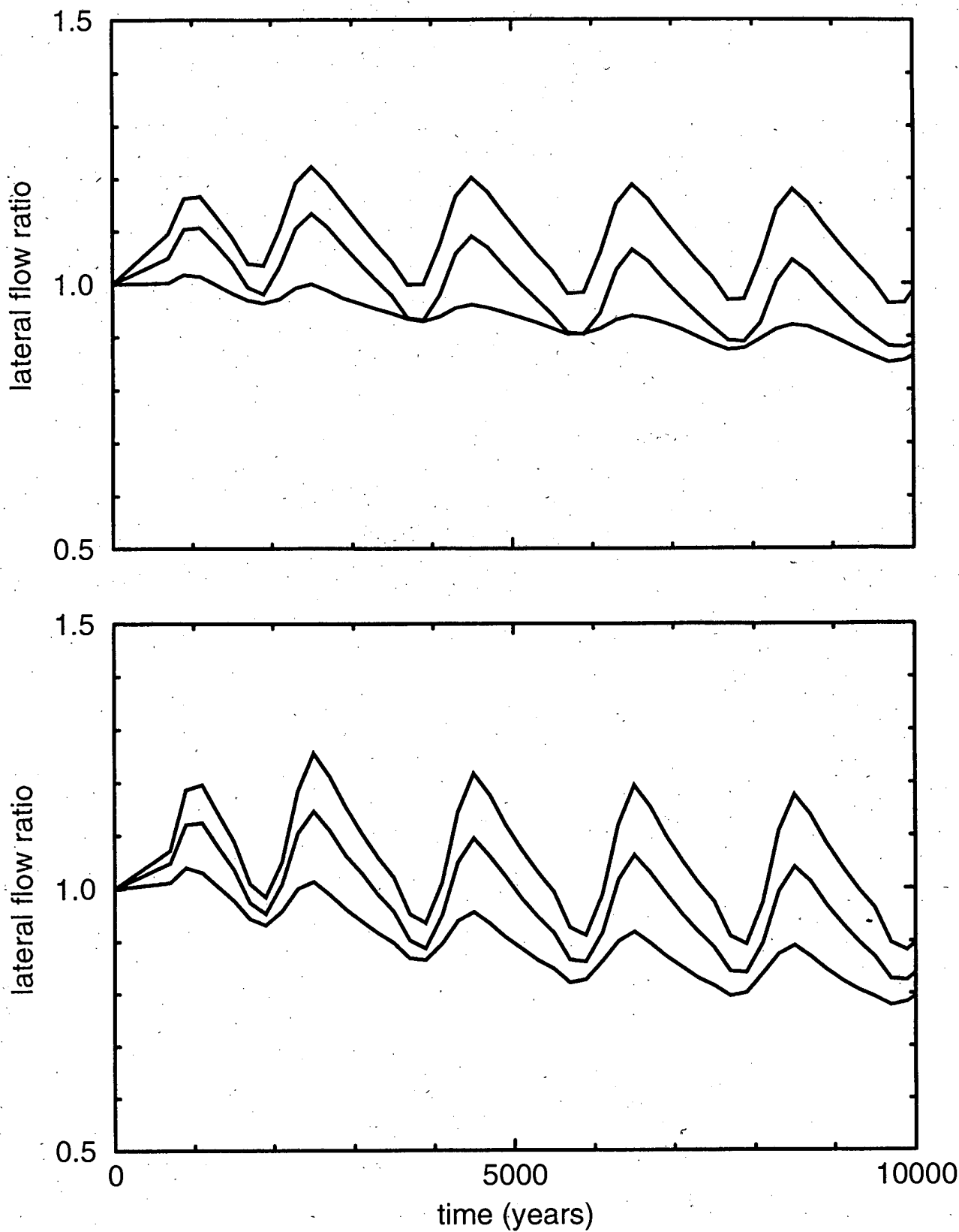


Figure 10. Lateral-flow ratio versus time for simulations 41, 42, and 43 (top) and 44, 45, and 46 (bottom).

PART 2: ANALYSIS DOCUMENTATION

A. Quality Assurance Status

The analyses reported in this records package were initiated previous to 8 November 1995 and consequently do not follow QAP 9-1Revision 1. However, documentation of this work will follow the guidelines contained in Appendix B of QAP 9-1Revision 1. The results of these simulations do not provide direct input to WIPP performance assessment calculations. Therefore the computer code has not been qualified under QAP 19-1Revision 1 and the data are not qualified.

B. Roadmap to Supporting Information for this Record Package

Records Package: FEPs NS-8 and NS-9; SWCF-A:1.1.6.3:NQ:TSK:NS-8,NS-9. WPO numbers 30801, 30802, and 36671.

Records Package: Stratigraphic data used for the 3-D Rustler Formation hydrologic model; not completed.

Records Package: Contour maps used for the 3-D Rustler Formation hydrologic model; SWCF-A:1.4.1.3:QED:QA:Contour Maps of Rustler Formation; 3-D Rustler Model. WPO number 23212.

Records Package: Stratigraphic gridding and zone identification for the 3-D Rustler Formation hydrologic model; not completed.

Records Package: Source code, input and output files, and graphical results from 3-D Rustler Formation hydrologic model; not completed.

C. Identification of Individuals Who Performed the Work Reported in this Records Package

P. Swift compiled and interpreted climate data, provided rationale for projecting Holocene precipitation patterns into the future.

S. Askew, T. Corbet, and P. Knupp ran the simulations.

Corbet interpreted simulation results.

D. Training and Certification Requirements

Certification of Personnel Qualifications for Corbet, Swift, Knupp, and Askew are on file. Corbet and Swift were trained on QAP 9-1 Revision 1, QAP 9-2 Revision 1, and QAP 17-1

Revision 1.

E. Identification of Computer Software and Hardware

Analysis code: SECOFL3D V 1.9. (copy of FORTRAN code and executables included in this records package on magnetic tape)

Compiler: HP FORTRAN Version 9.00

Plotting and data presentation package: IDL V. 3.6 (commercial code)

The simulations were performed on three platforms. The platform used for each simulation is identified in the history file for each simulation.

Platform name: flowpath
Machine model: HP 9000 Model 720
Machine ID number: 33924131
Operating system release and version identifier: HPUX A.09.01

Platform name: aquitard
Machine model: HP 9000 Model 712/80
Machine ID number: 2000443057
Operating system release and version identifier: HPUX A.09.05

Platform name: basin
Machine model: HP 9000 Model 712/60
Machine ID number: 2011228760
Operating system release and version identifier: HPUX A.09.03

F. Identification of Inputs and Sources

The following input parameters are required to run these simulations: spatial distribution over the model domain of hydraulic conductivity (m/s), elevation of the bottom of the layer (m), specific storage (1/m), specific yield (dimensionless), and land surface elevation (m) for each of the 10 model layers. Also temporal variation of potential recharge (m/s) to applied uniformly over the model domain. The input files containing all values of these parameters for all simulations will be included in the records package: Source code, input and output files, and graphical results from 3-D Rustler Formation hydrologic model.

Elevations of each stratigraphic layer were assigned by overlaying the model grid on structure contour maps. The land surface elevations are from published topographic maps. The

process of generating the model stratigraphic input will be described in the Records Package: Stratigraphic gridding and zone identification for the 3-D Rustler Formation hydrologic model.

The extents of the zones representing post-depositional geologic processes were inferred from geologic data. A description of how these zones were delineated and how adjustments to hydraulic conductivity for each zone were assigned will be described in the Records Package: Stratigraphic gridding and zone identification for the 3-D Rustler Formation hydrologic model.

A value of $1 \times 10^{-5} \text{ m}^{-1}$ was assumed for the specific storage for all rock types. This value is representative of a rock with a compressibility of $1 \times 10^{-9} \text{ Pa}^{-1}$ and a porosity of 0.1.

The values for the hydraulic conductivity of intact rock for each rock type, the specific yield, and the recharge rate and temporal pattern were subjectively varied as part of the sensitivity analysis in these simulations. The values for these parameters are listed in Tables 1, 2, and 3.

G. Documentation of Review of Work

The Records Package, Contour maps used for the 3-D Rustler Formation hydrologic model; SWCF-A:1.4.1.3:QED:QA:Contour Maps of Rustler Formation; 3-D Rustler Model, was reviewed by an IRT in May 1995.

FEPs NS-8 and NS-9 Records Package; SWCF-A:1.1.6.3:NQ:TSK:NS-8,NS-9 was reviewed as part of Surveillance S-96-04 conducted on December 13 and 14, 1995. One technical observation was directed at this Records Package.

A copy of Form 430 for this package and associated memo starts on the next page.